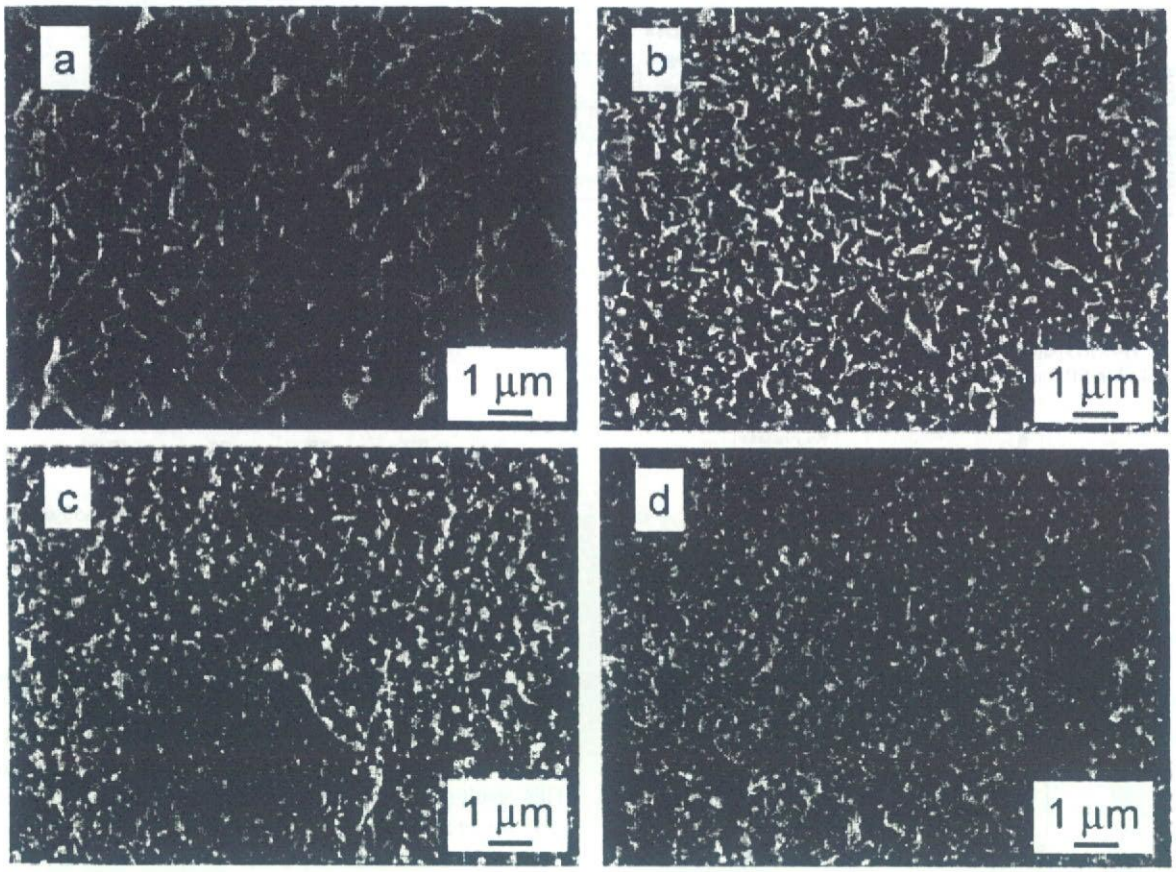

Fig. 3 Scanning electron micrographs of fracture surfaces of TiO_2/HDPE composites – 20 (a), 40 (b), 52 (c) and 55.6 vol% (d)

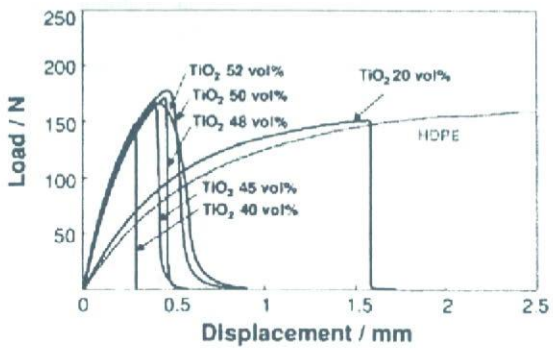

Fig. 4 Load-displacement curves for TiO_2/HDPE composites

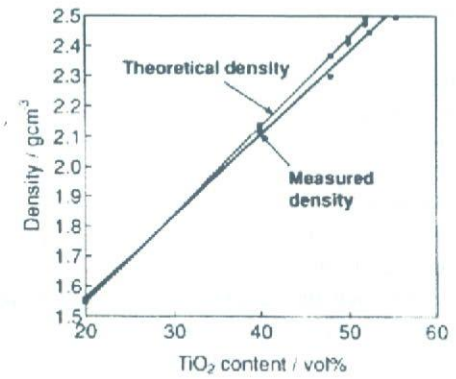

Fig. 5 Density of TiO_2/HDPE composites as a function of the TiO_2 content

Figure 9 shows FE-SEM photographs of the TiO_2/HDPE composite with 50 vol% of TiO_2 that was soaked in SBF at 36.5 C for various periods shorter than 14 days. No crystals were formed on the TiO_2/HDPE (Fig. 9b) surfaces after soaking in SBF for 5 days. The TiO_2/HDPE surface was covered with hemispherical particles around several micrometers in diameter after 7 days of soaking in SBF (Fig. 9c), and the number and size of the apatite nuclei increased with increasing soaking time (Fig. 9d). The morphology of the apatite on the TiO_2/HDPE composite was polycrystalline fine particles.

Discussion

The results shown here demonstrate that only the 20 vol% TiO_2 incorporation into the HDPE matrix was effective in enhancing the mechanical strengths of the HDPE. The reason for this effect is that the high mechanical strength of TiO_2 (Young's modulus 300–320 GPa) and its smaller particle size allow for a greater surface area to be available

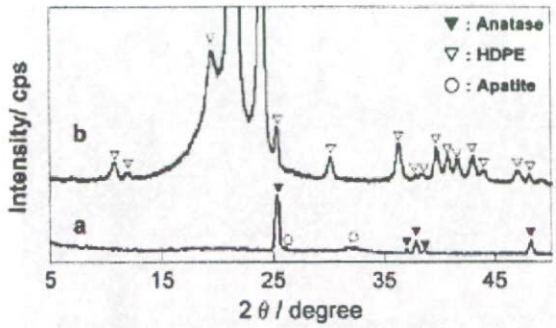

Fig. 6 TF-XRD patterns of the surfaces of TiO_2 particles (a) and HDPE (b) soaked in SBF at 36.5 °C for 3 and 14 days, respectively

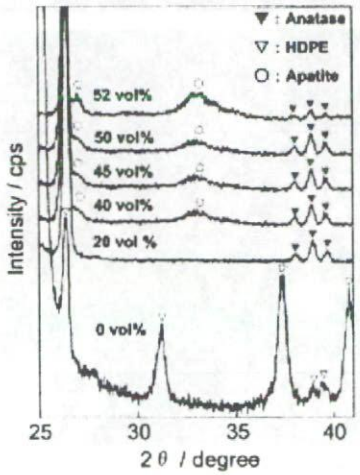

Fig. 7 TF-XRD patterns of the surfaces of TiO_2/HDPE –x composites soaked in SBF at 36.5 °C for 14 days (X = 0, 20, 40, 45, 50, 52 vol%)

for polymer/filler interaction and adhesion. The bending strength, yield strength and Young's modulus increased with increasing filler content, but they decreased when the filler content was greater than 52 vol%. Achieving a homogeneous dispersion of nanoparticles in a polymeric matrix is very difficult due to the strong tendency of nanoparticles to agglomerate [22]. Consequently, nanoparticle-filled polymers are liable to form a number of loosened clusters of particles. Figures 3c and d show TiO_2 aggregate in the HDPE matrix. These agglomerated for the composites with a TiO_2 content greater than 52 vol% and decreased the bending strength, yield strength and Young's modulus.

TiO_2/HDPE-20 and −40 also exhibited a much smaller plastic region after yielding, indicating that the interfacial bond between TiO_2 and HDPE was weak. As mentioned previously, TiO_2 nanoparticles (Fig. 1) had loosened clusters created by the aggregation of smaller TiO_2 particles this is shown in Figs. 3c and d. This structure caused a higher strain to failure due to an increase in crack deflection with increasing particle size of the composite with larger than 40 vol% TiO_2. For TiO_2/HDPE composites, no residual polyethylene

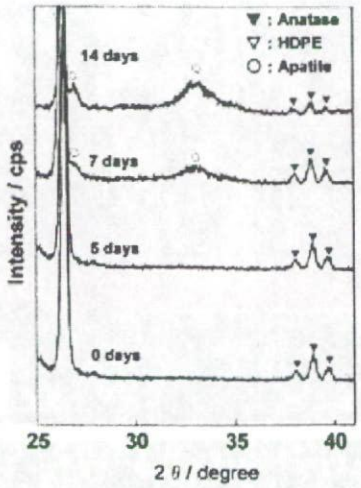

Fig. 8 TF-XRD patterns of the surfaces of TiO_2/HDPE-50 soaked in SBF at 36.5 °C for various periods

was found on the TiO_2 particle surfaces, indicating that no chemical bond existed between the matrix and filler (Fig. 3). Therefore, the voids form at the particle matrix interface, first in the direction of the applied stress (Fig. 5). This void then grows and merges as shear stresses deform the rest of the matrix, leading to the eventual failure of the composites. This result is consistent with the model proposed by Juhasz et al. for an apatite-wollastonite reinforced HDPE composite with no interfacial bonding [12].

Bonfield et al. developed hydroxyapatite-reinforced HDPE composite (HAPEX™) as an analogue material for bone replacement [7–10].The closer Young's modulus matching of the material to bone is an important factor in solving the problem of bone resorption. The fracture toughness and Young's modulus of HAPEX™ have a lower value than those of the human cortical bone.

The yield strength (50 MPa) and Young's modulus (7 GPa) for TiO_2/HDPE-40 were much larger than those for the HAPEX™ with 40 vol % of hydroxyapatite (28 MPa and 4.1 GPa, respectively). It has been generally observed that the addition of ceramic filler can substantially improve the mechanical strengths of the polyethylene. The mechanism of the reinforcing action is as follows. Inorganic fillers are actually bonded to the macromolecular chains and thereby immobilize the polymer chains. The degree of adhesion between the polymer matrix and fillers, the surface area of the filler, and the packing characteristics of the filler particles are important factors that determine the mechanical properties of the composites [23–25]. Comparing TiO_2 with hydroxyapatite as a ceramic filler, the surface area (8.56 m^2g^{-1}) and average particle size (535 nm) of TiO_2 were much larger and lower than those of hydroxyapatite [7] (7.61 m^2g^{-1} and 7.3 μm, respectively). TiO_2(40 vol%) homogeneously dispersed in the HDPE matrix via the kneading and compacting of TiO_2

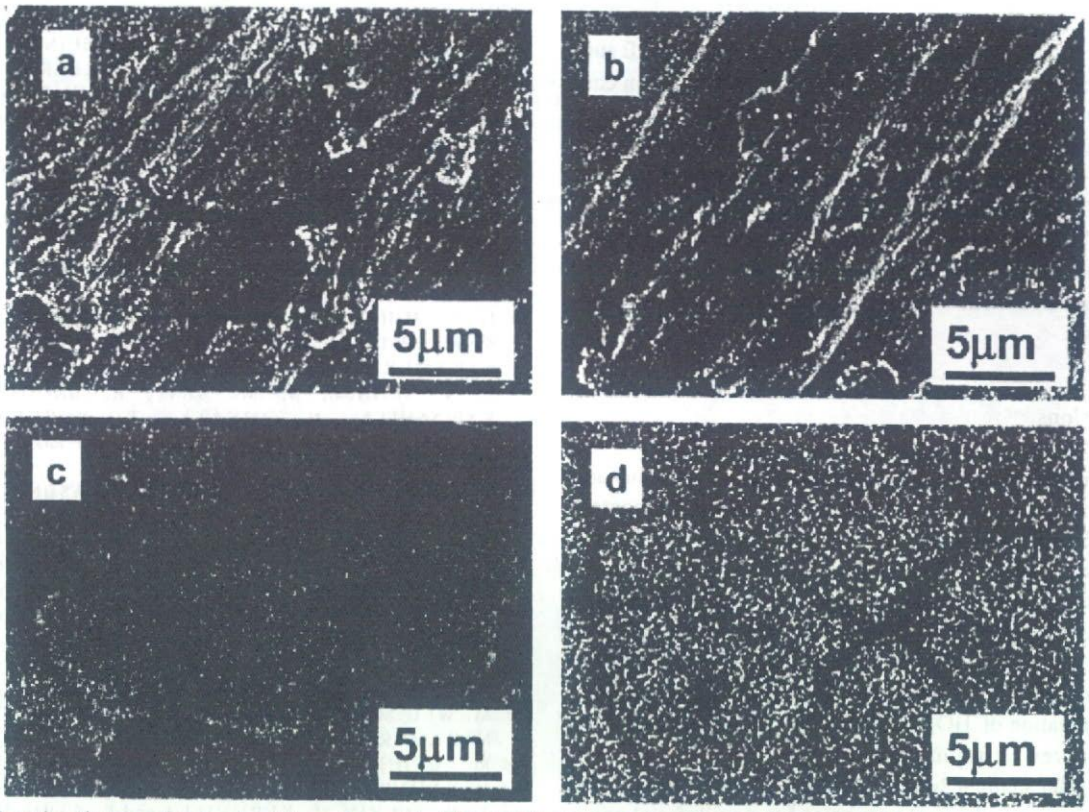

Fig. 9 Scanning electron micrographs of the surfaces of the TiO_2/HDPE-50 composite soaked in SBF at 36.5 °C for various periods: 0 days (a), 5 days (b), 7 days (c) and 14 days (d)

nanoparticles and HDPE (Fig. 3b). Many kinds of polyethylene exist, including ultrahigh molecular weight polyethylene (UHMWPE), HDPE and low density polyethylene (LDPE). Our previous study indicated that the degree of TiO_2 nanoparticle dispersion in the various polyethylene matrixes varied [26–28]. Therefore, the degree of homogeneous dispersion decreased in the order: HDPE (MFR8) > HDPE (MFR20) $\gg$ HDPE (MFR0.3) $\simeq$ HDPE (MFR40) $\gg$ UHMWPE $\simeq$ 0. These results indicate that the HDPE (MFR8) matrixes, in which TiO_2 nanoparticles with a high surface area are homogeneously dispersed have high mechanical properties, and that those with micrometer–sized hydroxyapatite particles eventually have low ones.

Biomineralization processes such as apatite formation are complex and involve the controlled nucleation and growth of apatite from aqueous solutions. Organisms create the proper organic matrix as a host for nucleation and growth, for control of solution concentrations, and for the supersaturation of precipitating phases. Most of the macromolecules known to promote surface nucleation contain functional groups that are negatively charged at pH's where the crystallization occurs [29].

In general, the crystallization of many sparingly soluble salts involves the formation of metastable precursor phases. In the case of calcium phosphate, various metastable phases have been identified. It is believed that the initial formation of an amorphous calcium phosphate may be followed by its transformation to hydroxyapatite. A recent X-ray diffraction crystallographic study by Kokubo showed that the anatase gel induces apatite formation the most effectively, followed by the rutile gel; the amorphous gel, however, forms no apatite [18]. The Ti-OH groups on the anatase gel combine with Ca^{2+} ions in the SBF to form amorphous calcium titanate. This calcium titanate later combines with phosphate ions in the SBF to form amorphous calcium phosphate with a low Ca/P ratio [30, 31]. The calcium phosphate transforms into the apatite, which exhibits a Ca/P ratio of 1.65. This demonstrates that the surface functional groups, which are capable of binding soluble ionic precursors, may become sites for surface nucleation.

The XRD study showed that the apatite formed on all the TiO_2/HDPE composites except for those with 0 and 20 vol % of TiO_2 as exemplified by the composite with 52 vol% of TiO_2 shown in Fig. 7. The induction period of the apatite nucleation was 7 days, as shown in Fig. 8. The as-received TiO_2 has an anatase structure, a Ti-OH group (Fig. 2) and a negative zeta potential (−22.5 mV). Figure 6 shows the apatite formed on the TiO_2 particles after soaking in SBF for as

little as 3 days; however no apatite formed on the polyethylene after soaking in SBF for 14 days. The TiO_2/HDPE surfaces were ground to a 30 μm finish with #400 silicon carbide abrasive paper. This suggests that the HDPE polymer chains were elongated and partially covered the surfaces of the TiO_2 particles. Therefore, the induction period of the apatite formation would be delayed for a longer time than that for TiO_2 particles. To enhance the apatite forming ability of the TiO_2/HDPE composite, it is necessary to remove by surface treatment the polyethylene that covers the TiO_2 particles.

Conclusions

The bending strength, yield strength, Young's modulus and compressive strength increased with increasing TiO_2 content up to 52 vol% (maximum bending strength = 68 MPa, yield strength = 54 MPa, Young's modulus = 7 GPa and compressive strength = 82 MPa). The strain to failure was reduced with increasing TiO_2 up to 40 vol%. However, as the filler content was increased from 45 to 52 vol%, the strain to failure increased due to the larger particle size resulting from the aggregation of TiO_2 nanoparticles. Three–point bending and compressive testing demonstrated that the composites with a filler content between 40 and 50 vol% showed the most suitable mechanical properties for maxillofacial applications. Apatite formed on TiO_2/HDPE that had greater than 40 vol% of TiO_2 after soaking in SBF for 7 days. These results indicate that the TiO_2/HDPE-50 composite is the most promising material in the present study for use as a load–bearing bone substitute.

Acknowledgements This work is in part supported by the National Research & Development Programs for Medical and Welfare apparatus from the New Energy and Industrial Technology Development Organization (NEDO) entrusted to the Japan Fine Ceramics Center.

References

1. L. L. HENCH, R. J. SPLINTER, W. C. ALLEN and T. K. JR. GREENLEE, *J. Biomed. Mater. Res.* **2** (1971) 117.
2. M. JARCHO, J. L. KAY, R. H. GUMAER and H. P. DROBECK, *J. Bioeng.* **1** (1977) 79.
3. T. KOKUBO, M. SHIGEMATSU, Y. NAGASHIMA, M. TASHIRO, T. NAKAMURA, T. YAMAMURO and S. HIGASHI, *Bull. Inst. Chem. Res. Kyoto Univ.* **60** (1982) 260.
4. S. NISHIGUCHI, H. KATO, H. FUJITA, H. M. KIM, F. MIYAJI, T. KOKUBO and T. NAKAMURA, *J. Biomed. Mater. Res.* **48(5)** (1999) 689.
5. S. FUJIBAYASHI, T. NAKAMURA, S. NISHIGUCHI, J. TAMURA, M. UCHIDA, H. M. KIM and T. KOKUBO, *J. Biomed. Mater. Res.* **56(4)** (2001) 562.
6. C. A. VAN BLITTERSWIJK, D. BAKKER, H. LEENDERS, J. BRINK, S. C. HESSELING, Y. P. BORELL, A. M. RADDER, R. J. SAKKERS, M. L. GAILLARD, P. H. HEINZE and G. J. BEUMER, ed. by P. Ducheyne, T. Kokubo and C. A. Van Blitterswijk, (Reed Healthcare Communications, The Netherlands, 1992) p. 13.
7. W. BONFIELD, M. D. GRYNPAS, A. E. TULLY, J. BOWMAN and J. ABRAM, *Biomaterials* **2** (1981) 185.
8. M. WANG, R. JOSEPH and W. BONFIELD, *Biomaterials* **19** (1998) 2357.
9. M. WANG and W. BONFIELD, *Biomaterials* **22** (2001) 1311.
10. M. WANG, *Biomaterials* **24** (2003) 2133.
11. J. A. JUHASZ, S. M. BEST, W. BONFIELD, M. KAWASHITA, N. MIYATA, T. KOKUBO and T. NAKAMURA, *J. Mater. Sci: Mater. In Med.* **14** (2003) 489.
12. J. A. JUHASZ, S. M. BEST, R. BROOKS, M. KAWASHITA, N. MIYATA, T. KOKUBO, T. NAKAMURA and W. BONFIELD, *Biomaterials* **25** (2004) 949.
13. T. FURUKAWA, Y. MATSUSUE, T. YASUNAGA, Y. NAKAGAWA, Y. OKADA, Y. SHIKINAMI, M. OKUNO and T. NAKAMURA, *J. Biomed. Mater. Res.* **50** (2000) 410.
14. L. L. HENCH and J. WILSON, in "An introduction to bioceramics" (World Scientific Publishing Co. London, 1992) p. 12.
15. T. KOKUBO, H. KUSHITANI and S. SAKKA, *J. Biomed. Mater. Res.* **24** (1990) 721.
16. M. UCHIDA, H. M. KIM, T. KOKUBO and T. NAKAMURA, *J. Am. Ceram. Soc.* **84** (2001) 2969.
17. M. WEI, M. UCHIDA, H. M. KIM, T. KOKUBO and T. NAKAMURA, *Biomaterials* **23** (2002) 167.
18. M. UCHIDA, H. M. KIM, T. KOKUBO and T. NAKAMURA, *J. Biomed. Mater. Res.* **64A** (2003) 164.
19. T. P. SELVIN, J. KURUVILLA and T. SABU, *Materials Letters* **58** (2004) 281.
20. N. E. DOWLING, in "Engineering materials for deformation, fracture and fatigue" (Prentice-Hall Inc. Englewood Cliffs, NJ; 1993), p. 570.
21. T. NAKAMURA, M. NEO and T. KOKUBO, in "Mineralization in Natural and Synthetic Biomaterials" ed. by P. Li, P. Calvert, T. Kokubo, R. Levy and C. Sheid (Materials Research Society, Warrendale, PA, 2000) p.15.
22. M. Z. RONG, M. Q. ZHANG, Y. X. ZHENG, H. M. ZENG, R. WALTER and K. FRIEDRICH, *Polymer* **42** (2001) 167.
23. Y. LIU, J. Y. LEE and L. HONG, *J. Power Sources* **109** (2002) 507.
24. C. J. R. VERBEEK, *Materials Letters* **57** (2003) 1919.
25. Z. WEN, T. ITOH, T. UNO, M. KUBO and O. YAMAMOTO, *Solid State Ionics* **8916** (2003) 1.
26. M. HASHIMOTO, H. TAKADAMA, M. MIZUNO, Y. YASUTOMI and T. KOKUBO, *Key Engineering Materials* **240–242** (2003) 415.
27. H. TAKADAMA, M. HASHIMOTO, Y. TAKIGAWA, M. MIZUNO, Y. YASUTOMI and T. KOKUBO, *Key Engineering Materials* **240–242** (2003) 951.
28. H. TAKADAMA, M. HASHIMOTO, Y. TAKIGAWA, M. MIZUNO, Y. YASUTOMI and T. KOKUBO, *Key Engineering Materials* **254–256** (2004) 569.
29. S. WEINER, *CRC Crit. Rev. Biochem.* **20** (1986) 365–408.
30. H. TAKADAMA, H. M. KIM, T. KOKUBO and T. NAKAMURA, *J. Biomed. Mater. Res.* **55** (2001) 185.
31. H. TAKADAMA, H. M. KIM, T. KOKUBO and T. NAKAMURA, *J. Biomed. Mater. Res.* **57** (2001) 441.

Electron gun using carbon-nanofiber field emitter

Y. Sakai, A. Haga, S. Sugita, S. Kita,[a] S.-I. Tanaka,[b] and F. Okuyama
Graduate School of Engineering, Nagoya Institute of Technology, Gokiso-cho, Showa-ku, Nagoya 466-8555, Japan

N. Kobayashi
Toshiba Corporation, 8 Shinsugita-cho, Isogo-ku, Yokohama 235-8523, Japan

(Received 27 September 2006; accepted 9 December 2006; published online 30 January 2007)

An electron gun constructed using carbon-nanofiber (CNF) emitters and an electrostatic Einzel lens system has been characterized for the development of a high-resolution x-ray source. The CNFs used were grown on tungsten and palladium tips by plasma-enhanced chemical-vapor deposition. Electron beams with the energies of $10<E<20$ keV were focused by the electrostatic lens and impinged on a W target for x-ray radiography. Analyzing the recorded x-ray radiographs, the focal spot size of the electron beam extracted from the CNFs was estimated to be $D<50$ μm in diameter. Superior performance was realized by using CNFs with larger fiber radii (100–500 nm) grown sparsely on the metal tips, which were installed in a holder at the short length $L=0.5$ mm. © *2007 American Institute of Physics.* [DOI: 10.1063/1.2430650]

I. INTRODUCTION

In recent years, carbon nanofibers[1] (CNFs) and carbon nanotubes[2] (CNTs) have been widely used as field electron emitters, due to their excellent physical and chemical properties, such as their small tip radius of curvature, high aspect ratio, mechanical toughness, and chemical stability. Although there is no strict classification between the CNTs and CNFs,[3] nanofibers with diameters ranging from 30 to 1000 nm are tentatively classified as CNFs. Since high-resolution transmission electron microscopy has revealed no parallel (001) fringes on the fiber sidewalls, our fibers might be more rodlike than tubular. Electrons extracted through field emission (FE) processes from the CNTs and CNFs have been successfully applied to x-ray sources.[4–7] X-ray radiography (XR) has been used over a broad area of medicine and industry. In XR, a small source size of x ray is required to obtain high-resolution images. Since field emission provides a narrower energy distribution of electrons and a smaller emission area, the field electron emitter is expected to be suitable for focusing electron beams into a small spot. Thus, the CNF and CNT emitter will make it possible to develop a high-resolution x-ray source operating in a nonultrahigh vacuum. To develop a high-resolution x-ray source using an electrostatic lens system, one has to fully understand the field emission and focusing characteristics of electron beams. Microfocused x-ray tubes with CNT emitters have recently been reported.[8,9] Our previous study concerning the FE from CNFs grown on Pd wire indicates that CNFs with diameters larger than 100 nm provide intense and stable emission current.[10] In this study, field emission processes from the CNFs grown on etched metal (W and Pd) tips have been extensively investigated, and focusing of electron beams with energies of $10<E<20$ keV extracted from the CNFs was studied by inspecting x-ray radiographs.

II. EXPERIMENT

The CNFs were grown on etched tungsten (W) and palladium (Pd) tips by the plasma-enhanced chemical vapor deposition (PECVD) method.[11] The metal tips were prepared by electrochemical etching of 0.5 mm diameter wires. The etching was performed in 1 mol KOH solution for W and in H_3PO_4 solution for Pd. The W tips prepared in this way usually had radii of curvature of 1–2 μm, while the Pd tips had radii of curvature of 3–20 μm because of greater difficulty in the etching.

In the case of the W tips, after ultrasonic cleaning, a palladium (Pd) film serving as a catalyst of CNF growth was deposited on the tip by argon sputtering of a Pd disk. The film thickness was approximately 100 nm. CVD gases in the CNF growth were acetylene (C_2H_2) at a pressure of 60 Pa and ammonia (NH_3) at a pressure of 140 Pa. During CVD, the W tips were resistively heated, and the temperature of the substrates near the end of the tips was monitored with the aid of a radiation thermometer. By applying a negative dc voltage of 600 V to the heated tips for 20 min, CNFs could be synthesized on the tips. For the Pd tips, CNFs were grown directly on the tips in almost the same way as in W tips, but the CVD gas pressures were somewhat lower than those for W, i.e., 20 Pa for C_2H_2 and 40 Pa for NH_3. The morphology of CNFs thus prepared was determined by scanning electron microscopy (SEM).

The experimental setup employed in the present study is schematically shown in Fig. 1. The vacuum chamber was pumped down to 1.5×10^{-7} Pa with both a turbo-molecular pump and an ion pump. By applying negative high voltage to the as-grown CNF emitter, FE electrons were extracted from the CNFs. In our measurements, no preheating of the CNF

[a]Author to whom correspondence should be addressed; electronic mail: s.kita@nitech.ac.jp
[b]Present address: Institute of Multidisciplinary Research for Advanced Materials, Tohoku University, 2-1-1 Katahira, Sendai 980-8577, Japan.

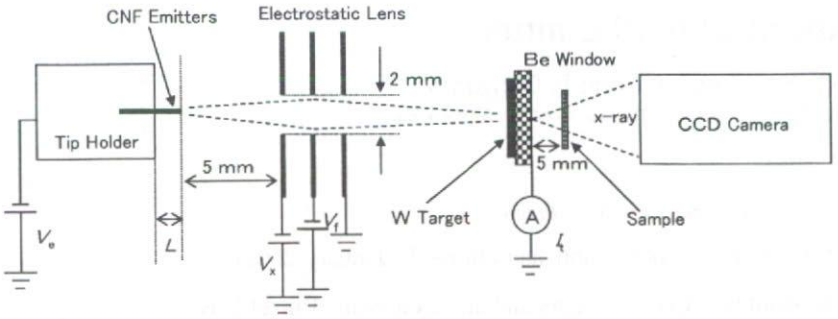

FIG. 1. Schematic drawing of apparatus used for characterization of electron beams extracted from CNF emitters.

emitter was attempted in order to remove the catalyst Pd particles. The electron beam extracted from the CNFs was accelerated to a desired energy of 10–20 keV and focused on the W-target by the electrostatic lens. Bombarding the W-film target (1 μm in thickness) with the focused electron beam, x rays were made to radiate from the target. They passed through a beryllium (Be) window with a thickness of 200 μm and escaped into the atmosphere. X-ray images of the samples were recorded by a charge-coupled device (CCD) camera, with a resolution of about 80 μm/pixel. The electrostatic lens system consisted of three parallel electrodes. The first one in the lens was also used as an extractor electrode, the second one for focusing, and the third corresponded to an accelerated electrode. Each electrode was separated every 3 mm by ceramic spacers and was perforated in diameter 2 mm at the center. The W target was located at a position 10 cm apart from the CNF emitter, which was fixed in a metallic tip holder and placed 5 mm away from the extractor electrode. The distance L between the end of the tip and the holder indicated in Fig. 1 was varied, which allowed us to investigate the emission and focusing properties of electron beams as a function of L. In this study, the characteristics of field electron emissions from the CNFs were measured extensively, and the spot size of the focused electron beams was estimated by measuring the resolution of x-ray radiographs.

III. RESULTS AND DISCUSSION

Figure 2 shows the SEM images of the CNF emitters used in this study. Figures 2(a) and 2(b) exhibit CNFs grown on etched W tips at the substrate temperatures of 400 and 800 °C, respectively. As seen in the figures, the CNFs were grown on the entire substrate surface and were well aligned, but their diameters depended on the substrate temperatures. As estimated from these images, the CNFs grown at 400 and 800 °C were 50–100 and 200–600 nm in diameter, respectively. Thus, the CNFs grown at higher temperatures on the W tips had larger diameters. Figure 2(c) shows the SEM images of CNFs grown around 700 °C on an etched Pd tip. Those CNFs had diameters of 50–1000 nm and were grown vertically from the substrate surface and sparsely distributed at the end of the Pd tip. These results may suggest that the sputter deposition of catalyst film leads to relatively uniform CNF growth. Since the catalyst nanoparticles were always observed at the top of CNFs, they presumably grew through the so-called tip-growth mechanism.[1]

The emission characteristics of the CNF emitters described above are exhibited in Fig. 3. Figure 3(a) shows the total emission current I measured as a function of the voltage V applied to the emitter. The measurements were performed for the tip lengths of L=3 and 0.5 mm (see Fig. 1) without operating the electrostatic lens (V_f=0 Fig. 1). In the figure, curves 1–3 are the data at L=3 mm, and curves 1′–3′ are those at L=0.5 mm. Curves 1 and 1′ correspond to the CNF emitter in Fig. 2(a), curves 2 and 2′ to that in Fig. 2(b) and curves 3 and 3′ to that in Fig. 2(c). The total emission cur-

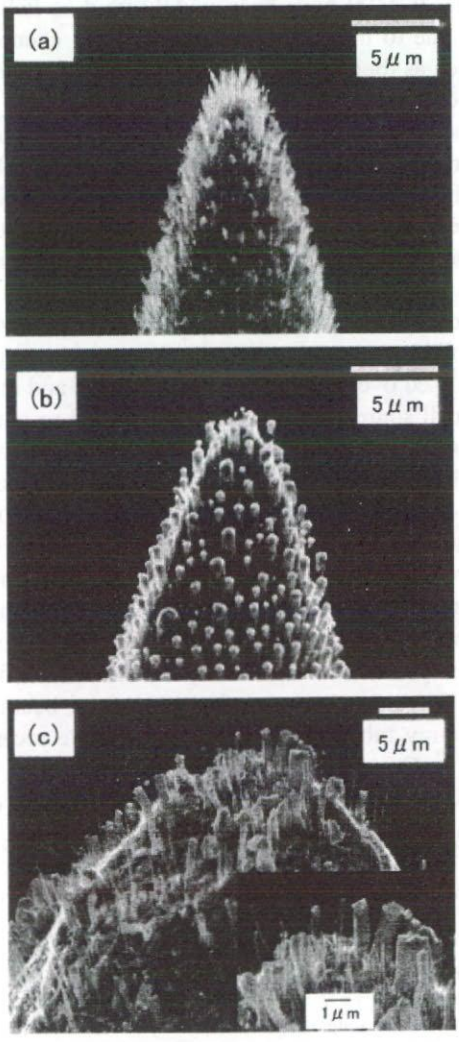

FIG. 2. SEM images of CNFs grown on metal tips. (a) CNFs on W tip at 400 °C (emitter 1). (b) on W tip at 800 °C (emitter 2). (c) CNFs on Pd tip (emitter 3). Inset shows image around top of emitter.

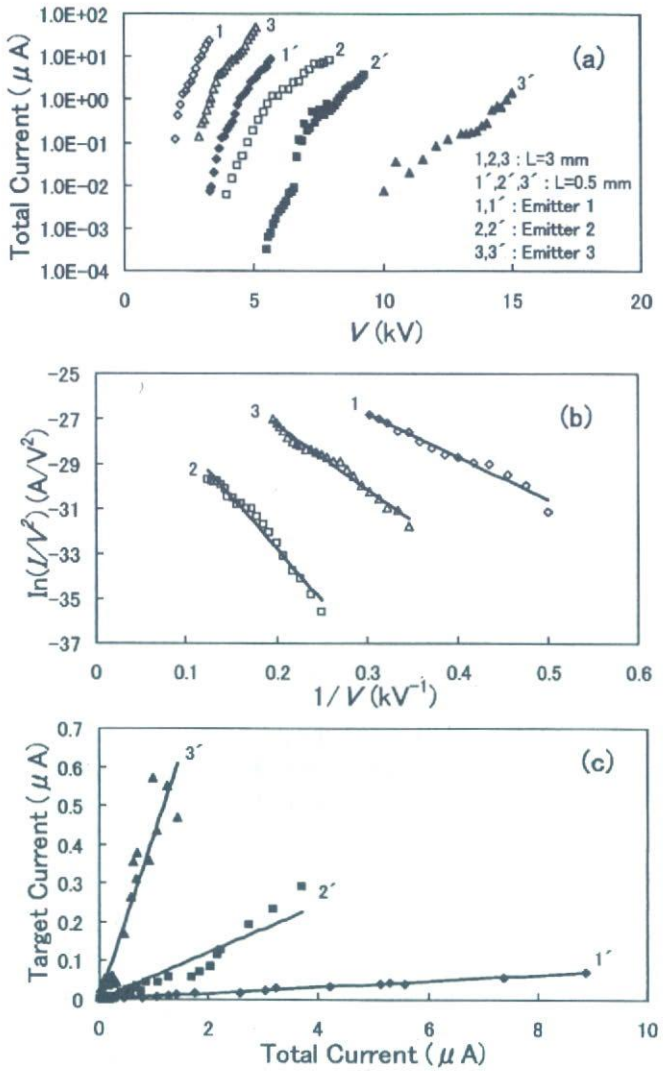

FIG. 3. Field emission characteristics of CNFs. (a) Current-voltage (I-V) curves measured for tip length L=3 and 0.5 mm. Curves 1–3 are for L=3 mm, and curves 1′–3′ are for L=0.5 mm. Curves 1 and 1′ are for emitter 1, curves 2 and 2′ for emitter 2, and curves 3 and 3′ for emitter 3. (b) FN plots for total current, and (c) relation between target current I_t and total current I.

rent was measured up to 50 μA. In all the curves, the current exponentially increased with elevations in the applied voltage V. As the figure makes clear, the magnitude of the field emission current strongly depends on the tip length L, and the voltages V for the L=0.5 mm are 1.5–4 times higher than those for L=3 mm. The L dependence is especially pronounced for the CNF emitter on the Pd tip. With any decrease in L, the electric field around the CNFs is strongly suppressed by the tip holder shown in Fig. 1. Hence, higher applied voltages are necessary to obtain certain emission currents. This L dependence of electric field strength is more effective in the emitter with a large radius of curvature R_0 at the tip end, which might be the reason underlying the strong L dependence of the I-V characteristics for the Pd tip in Fig. 3(a), the radius R_0 of which was as large as 14 μm. The L dependence could not be observed at $L>1$ mm, but was strong at $L<1$ mm. According to our simple estimation, this L dependence can be roughly presented by $V \sim V_0[1+A(R_0/L^4)]$ where V_0 is voltage for a certain intensity at $L>1$ mm, and the constant A is given by 1.5×10^{-8} m^3.

Another remarkable fact about the experimental I-V curves 1–3 is that the applied voltages V for the emitter on Pd (curve 3) with a radius of curvature of R_0=14 μm were appreciably lower than those for the W tip (curve 2) with a small radius of R_0=2 μm, possibly suggesting that the electric field depends not only on the R_0 but also critically on the surface structure around the CNFs. Here we would like to focus our discussion on the experimental results at L =3 mm, aside from the L dependence on the applied voltage V discussed above. An analysis using the well-known Fowler-Nordheim (FN) theory[12] provides valuable information on the local electric field on the CNFs surface. Figure 3(b) gives the FN plots [$\ln(I/V^2)$ vs $1/V$] evaluated from the experimental I-V curves 1–3 in Fig. 3(a). Since all the plots lie along nearly straight lines, one can approximately evaluate the local electric field F on the CNFs from the slopes of these lines. According to our approximate calculations of the electric field around the substrate tip, which was assumed to have a semispherical structure with the radius R_0 on a cylindrical shank, a macroscopic electric field E on the tip can be given by $E \sim V/2R_0$ for the radius $1 \leqq R_0 \leqq 20$ μm.[13] Using the proportionality factor β giving field enhancement, the local field F on the CNFs is given by $F=\beta E=\beta V/2R_0$ Slope α of the line in the FN plot is given by $\alpha=1.36 \times 10^7 R_0 \Phi^{3/2}/\beta$ [kV],[12] where Φ denotes the work function of the CNFs, with R_0 in meters. The theoretical and experimental values of Φ reported so far for CNTs range from 4.2 to 5.1 eV.[14–18] This wide discrepancy might be due to differing respective evaluations of the CNT surface state. The FE electrons are considered to be emitted not only from the CNFs but also partly from the catalyst Pd on top of our CNFs. The work function of the Pd is approximately 5.1 eV.[19] Therefore, we may employ Φ=5.0 eV in our analysis, a value nearly common to both CNTs and Pd. By assuming a work function of Φ=5.0 eV, the enhancement factors are $\beta \sim 14$ for emitter 1, $\beta \sim 6$ for emitter 2, and $\beta \sim 75$ for emitter 3. The local electric field largely depends on the growth density of CNFs; the electric field around a CNF in a densely populated area is strongly shielded by adjacent fibers.[17] This may be the reason why β varied from emitter to emitter. The $\beta \sim 75$ for the Pd tip was much larger than those for W tips. The remarkably lower applied voltages in the I-V curve 3 in Fig. 3(a) for the CNF emitter on the Pd tip is due to a larger enhancement factor of $\beta \sim 75$. As seen in the SEM images of Fig. 2, the CNFs on the Pd tip (emitter 3) have a lower density and a larger diameter size than those on the W tips (emitters 1 and 2). These findings should confirm the origin of the larger value of $\beta(\sim 75)$ for emitter 3.

To develop a fine-focusing x-ray source, one needs an electron beam with a higher brightness. The brightness is given by $B=J/\Omega$, where J and Ω are electron density and a solid angle for the beam spread, respectively. Figure 3(c) shows the beam intensity I_t measured at the target located behind three electrodes for the lens system in Fig. 1. These are the results for the tip length of L=0.5 mm. The ordinate in this figure indicates the beam intensity I_t and the abscissa

shows the total emission current I. The experimental results in Fig. 3(c) suggest that the beam intensity I_t is nearly proportional to the total current I, allowing one to immediately estimate the transmission rate of $\gamma=dI_t/dI$ from the slope of these lines. The rates γ evaluated from the data in Fig. 3(c) were 0.008 for emitter 1 on W tip at 400 °C, 0.06 for emitter 2 on the W tip at 800 °C, and 0.35 for emitter 3 for the Pd tip. Thus, the transmission rate for CNF emitter 3 on the Pd tip was especially large, whereas the rate for emitter 3 measured at $L=3$ mm was approximately $\gamma=0.03$, which was much smaller than the $\gamma=0.35$ at $L=0.5$ mm, confirming that the transmission rate γ can be appreciably enhanced by decreasing the tip length L. To interpret the experimental results, the FE patterns for emitter 3 have been observed using a phosphor screen installed in another ultrahigh vacuum chamber. According to the subsequent experiments, the angular spread of the FE electron for the tip length of $L=0.5$ mm was 1/3 smaller than that for $L=3$ mm. This is why the transmission rate for emitter 3 was appreciably increased by reducing the tip length L. These results for emitter 3 on the Pd tip indicate that the CNFs grown sparsely on the metal tip with a larger radius R_0 provide a well-aligned electron beam. Since the spot size D of the focused electron beam strongly depends on the spread angle $\Delta\theta$, $D \propto (\Delta\theta)^3$,[20] the CNF emitter on the Pd tip might have a small spread angle $\Delta\theta$, and is expected to provide a focused beam of a smaller spot size and a higher resolution for x-ray radiography.

Using the spread half-angle $\Delta\theta$, beam intensity I, and effective emitting area S, the brightness B for the circular beam is written by $B=J/\Omega=I/[\pi S(\Delta\theta)^2]$. According to additional observations by a phosphor screen, FE patterns are composed of countable numbers of bright spots, and the distinguishable spots typically have spread half-angle of $\Delta\theta \sim 60$ mrad, which is nearly the same as the previous observation.[10] Accordingly, one cannot directly determine the effective emitting area S. For an electron emitter composed of a single CNT, the effective emitting area S has been successfully evaluated using the FN formula.[18] In this study, as a trial evaluation, we have determined the S by analyzing the I-V curves with the FN formula. The constant value A determining the magnitude of the ordinate $\ln(I/V^2)$ in the FN plot [see Fig. 3(c)] is given by $A=\ln(3.85\times10^{-7}\beta^2 S/\Phi R_0^2)$. The spread angles $\Delta\theta$ of the electron beams were estimated to be about 100 mrad for emitters 1 and 2, and 90 mrad for emitter 3, which will be discussed later. The brightness evaluated at the maximum applied voltage V is approximately given by 7×10^{11} A/(m^2 sr) for emitters 1 and 2, and 8×10^{12} A/(m^2 sr) for emitter 3, respectively. Thus, emitter 3 has the largest brightness B among the emitters characterized in this study, and is expected to give the best x-ray radiography performance. The brightness $B=8\times10^{12}$ A/(m^2 sr) for emitter 3 gives the reduced brightness $B_r=B/V=6\times10^8$ A/(m^2 sr V), which is somewhat lower than the values of $B_r=(1.3-2.5)\times10^9$ A/(m^2 sr V) reported in the early studies using CNTs.[17]

Luminescence on a phosphor screen originated by electron impact was first used to observe the focusing character of the electrostatic lens system. For this experiment, the W target in Fig. 1 was replaced by the phosphor screen. The focusing voltage V_f applied to the second electrode in the lens system was approximately determined through the observation of luminescence on the screen. For the acceleration voltage of $V_a=15$ kV$(=-V_e)$, the focusing voltage yielding the minimum spot size was $V_f\sim-11$ kV $(V_f/V_e\sim0.73)$, which was weakly dependent on the extraction voltage $\Delta V=V_x-V_e$ (changed by the emitter). The optimal focusing voltage V_f was finally determined by observing the x-ray radiographs for each experimental condition of the emitter, the extraction voltage, and the accelerating voltage. The intensity of electron beams impinging on the W target was almost the same as those given in Fig. 3(c).

Figure 4 shows the x-ray images of a test chart composed of lead (Pb) lines with their line profiles measured to evaluate the spot size D in diameter of the focused electron beams. Under our experimental condition, electron spot size is considered to be nearly equal to the focal size of x ray radiated from the W target. By taking x-ray images of the vertical and horizontal Pb lines, the spatial resolution of an x-ray source can be estimated. Figures 4(a) and 4(b) show the x-ray images for emitters 1 and 2 on the W tips, respectively. The exposure time for these images was 180 s. The width of the observed Pb line in Fig. 4(a) for emitter 1 was 62.5 μm. The three stripes in the figure are sufficiently separated. The Pb linewidth in Fig. 4(b) for emitter 2 was 50 μm, and the three stripes here are also well separated. As a result of those measurements, the spatial resolution on the x-ray images was estimated to be roughly 55 and 40 μm for CNF emitters 1 and 2, respectively, on the W tips. Figure 4(c) also exhibits an x-ray image of Pb lines 50 μm in width and its line profiles for emitter 3 on the Pd tip. The exposure time for this image was 300 s. As can be seen in the figure, the three stripes are quite well separated. By analyzing the blur structure of the Pb line edge in the x-ray image,[21] the spot sizes D for emitters 1, 2, and 3 were evaluated as approximately 60, 50, and 40 μm, respectively. As the next step, the x-ray image of Fig. 4(c) was simulated by assuming the circular intensity distribution given by $I=I_0\exp(-1.7\times10^9 r^2)$, where I_0 is a proportionality constant, and r is the distance in meters with respect to the beam axis. As a result of the simulation, the spatial resolution on the x-ray image was evaluated as approximately 25 μm for emitter 3. The performance of emitter 2 on the W tips was somewhat poorer than that of emitter 3. If emitter 2 was used with a smaller tip length than $L=0.5$ mm, e.g., $L=0.25$ mm, better performance would result. Since the CNF emitter 3 on the Pd tip and emitter 2 on the W tip delivered superior performance, they may be used as an electron source for a high-resolution x-ray tube.

For further understanding of the focusing action by an electrostatic lens, focal-spot sizes for the used FE emitters have been simulated by employing a simple model program,[13] which calculates trajectories of FE electrons and makes for broadening of focal-spot size due to spherical aberration. The simulated results only weakly depend on the radius of curvature R_0 at the tip end, and the focus-size diameter for the emitters used in this study is approximately given by $D_{\text{th}}=0.054(\Delta\theta)^3$ m, where $\Delta\theta$ is in units of radian. Connecting this calculated D_{th} and the experimental beam

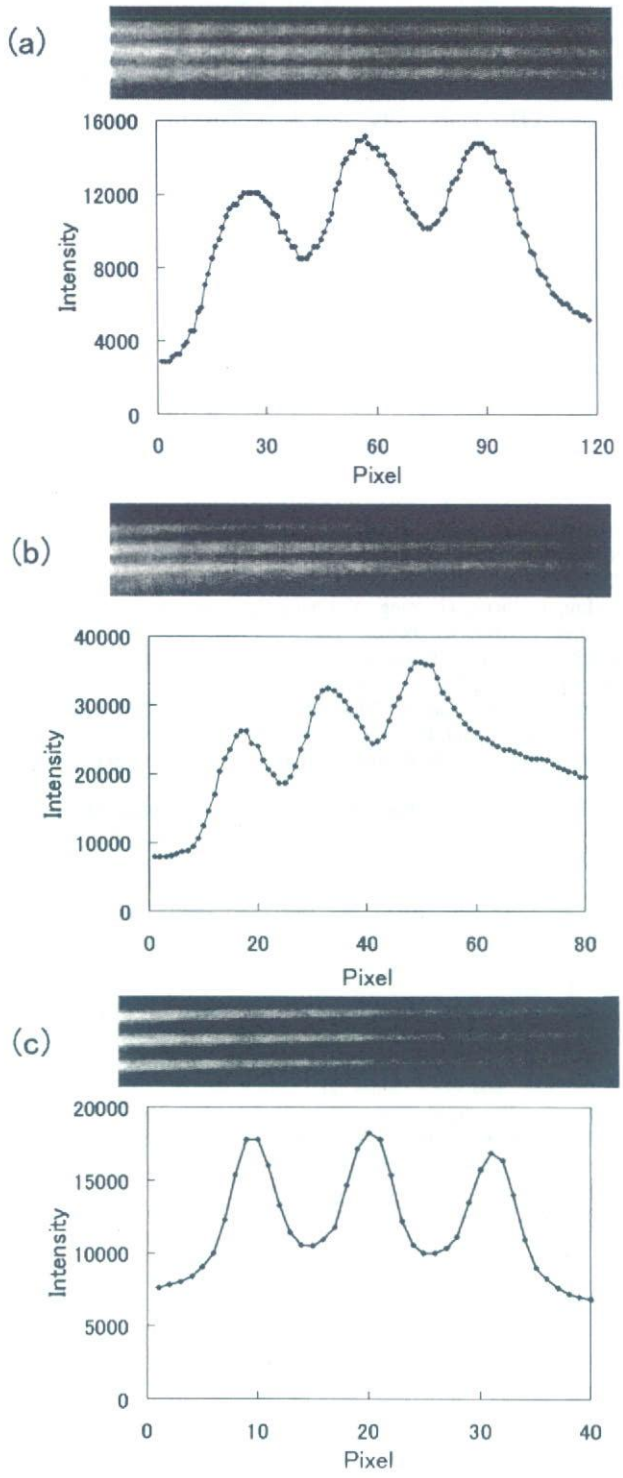

FIG. 4. X-ray images of test charts and their line profiles for electron beams extracted from CNF emitter at acceleration voltage of V_a=15 kV. (a) For CNF emitter 1 on the W tip at 400 °C. Stripe width is 62.5 μm. (b) For emitter 2 on W tip at 800 °C. Stripe width is 50 μm. (c) For emitter 3 on Pd tip. Stripe width of test chart is 50 μm.

sizes determined in this study (D=60, 50, and 40 μm for emitters 1, 2, and 3, respectively), one can estimate the spread half-angle $\Delta\theta$ of the electron beams. The results are $\Delta\theta\sim$100 mrad for emitters 1 and 2, and $\Delta\theta\sim$90 mrad for emitter 3. According to the trajectory analysis, the electrons entering the electrostatic lens with the angle $\Delta\theta<$200 mrad can pass through the lens and reach the target. If one estimates focal size D^* using the maximum angle $\Delta\theta$ =200 mrad for the fully spread electron beam, one has D^* $\sim$400 μm, which is much larger than the experimental sizes of D=40–60 μm. Thus, performance of the electron gun is significantly improved by using FE electrons with narrow angular spread. For further improvement of the focusing, however, it is desirable to fabricate the electron gun by employing an electrostatic Einzel lens composed of asymmetric electrodes.[22] According to our computer analysis, the asymmetric Einzel lens provides a focal-spot size smaller by a factor 1/10 than those for the lens obtained here.[23] The asymmetric Einzel lens has been very recently applied to a microfocused x-ray source with CNT emitter,[24] which has better resolution than that for symmetric lens.[9]

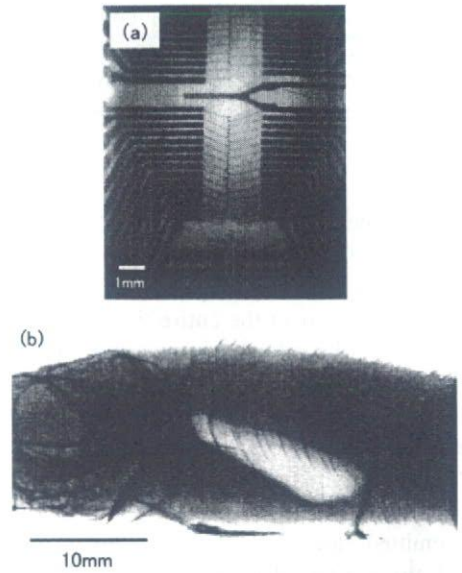

FIG. 5. Typical x-ray images taken with electron beam extracted from CNF emitter 3 on Pd tip. (a) LSI image (V_a=−15 kV, T=300 s), and (b) image of a small raw fish (V_a=13 kV, T=450 s).

Figure 5 shows typical x-ray images demonstrating the performance maintained with the electron beam extracted from CNFs grown on the Pd tip. For the LSI image shown in Fig. 5(a), its interior structure, such as Cu wires (~30 μm in width), could be readily observed nondestructively. The image of the small raw fish in Fig. 5(b) also sharply delineated such inner structures. X-ray images were also taken of the CNF emitter 2 on the W tip, and though not shown here, they are of nearly the same quality as those shown in Fig. 5. Thus, the images provided clear structural views of the biological as well as nonbiological materials. These results indicate that the CNF emitters grown on the etched metal tips can be successfully applied in the electron gun to develop a finely focused electron beam and a high-resolution x-ray source constructed with electrostatic and magnetic lenses.

Finally, we refer to the microfocused x-ray tubes using the CNT field emitter reported by other groups.[8,9,24] In their x-ray sources, electron emitters have been prepared in forms with a large diameter of 1–2 mm using CNT bundles, and provide intense electron emissions of around 1 mA, which is higher than the intensity in our electron gun. The x-ray spot sizes maintained in their sources are lower than 100 μm, which is comparable to our results. From the standpoint of

the beam intensity, the larger size of emitters thus assures better performance, while an x-ray source with fine resolution (i.e., nanofocusing) will be realized by using a smaller CNT and/or CNF emitters with higher brightness.

IV. SUMMARY

We have synthesized CNFs on etched W tips at substrate temperatures of 400 and 800 °C, and on etched Pd wire at 700 °C by the PECVD method. For the W tips, the CNFs were grown vertically over the entire tip with diameters that were dependent on the substrate temperature. For the Pd tip, the CNFs were grown sparsely and their average diameters exceeded those for the W tips. The performance of CNF field emitters equipped in the electron gun has been extensively evaluated by repeated experiments. As for the field emission characteristics, CNF emitter 1 on the W tip and emitter 3 on the Pd-tip emitted electrons at lower voltages, while emitter 2 on the W-tip emitted electrons at somewhat higher voltages. Among the three emitters used in this study, the CNF emitter 3 on the Pd tip had the highest transmission rate. To investigate the focusing characteristics of the electron beams extracted from the CNF emitters we also recorded the x-ray radiographs using a CCD camera. From x-ray images of the x-ray test chart and their line profiles, we have confirmed that the CNF emitter on the W-tip grown at 800 °C and on the Pd tip at 700 °C have a focal spot size of less than 50 μm. Better performance could be realized by using CNF emitters 2 and 3 with large fiber radii (100–500 nm) grown sparsely on the metal tips, which were installed in a holder at the short length $L=0.5$ mm. These CNF emitters would be suitable for an electron gun of a high-resolution x-ray source equipped with electrostatic and magnetic lens systems.

ACKNOWLEDGMENTS

The authors gratefully acknowledge Dr. Y. Okazaki, Y. Matsumoto, R. Kubota, and Y. Oga (Nagoya Institute of Technology, Nagoya, Japan) for their considerable contributions to this work. They are also greatly indebted to Professor O. Eryu (Nagoya Institute of Technology, Nagoya, Japan) for preparation of the W film target in XR. They would also like to thank Dr. S. Senda (Nagoya Institute of Technology, Nagoya, Japan), Dr. A. Yamaguchi, Dr. N. Aoki (Toshiba Corporation, Yokohama, Japan), and Professor M. Miyoshi (The University of Tokyo, Tokyo, Japan) for their valuable discussions. This study was financially supported by SENTAN, JST.

[1] A. Oberlin, M. Endo, and T. Koyama, J. Cryst. Growth **32**, 335 (1976).
[2] S. Iijima, Nature (London) **354**, 56 (1991).
[3] A. V. Melechko, V. I. Merkulov, T. E. McKnight, M. A. Guillorn, K. L. Klein, D. H. Lowndes, and M. L. Simpson, J. Appl. Phys. **97**, 041301 (2005).
[4] H. Sugie, M. Tanemura, V. Filip, K. Iwata, K. Takahashi, and F. Okuyama, Appl. Phys. Lett. **78**, 2578 (2001).
[5] G. Y. Yue, Q. Qiu, B. Gao, Y. Chang, J. Zhang, H. Shimoda, S. Chang, J. P. Lu, and O. Zhou, Appl. Phys. Lett. **81**, 355 (2002).
[6] T. Matsumoto and H. Mimura, Appl. Phys. Lett. **82**, 1637 (2003).
[7] S. Senda, Y. Sakai, Y. Mizuta, S. Kita, and F. Okuyama, Appl. Phys. Lett. **85**, 5679 (2004).
[8] K. Kawakita, K. Hata, and H. Sato, J. Vac. Sci. Technol. B **24**, 950 (2006).
[9] Z. Liu, J. Zhang, G. Yang, Y. Cheng, O. Zhou, and J. Lu, Rev. Sci. Instrum. **77**, 054302 (2006).
[10] S. Kita, Y. Sakai, T. Fukushima, Y. Mizuta, A. Ogawa, S. Senda, and F. Okuyama, Appl. Phys. Lett. **85**, 4478 (2004).
[11] M. Tanemura, K. Iwata, K. Takahashi, Y. Fujimoto, F. Okuyama, H. Sugie and V. Filip, J. Appl. Phys. **90**, 1529 (2001).
[12] R. H. Fowler and L. W. Nordheim, Proc. R. Soc. London, Ser. A **119**, 103 (1928).
[13] R. Kubota, A. Haga, J. Kawashima, and S. Kita (unpublished).
[14] S. Suzuki, C. Bower, Y. Watanabe, and O. Zhou, Appl. Phys. Lett. **76**, 4007 (2000).
[15] J. Zhao, J. Han, and J. P. Lu, Phys. Rev. B **65**, 193401 (2002).
[16] W. Y. Li, K. Goto, J. Takioto, S. Tanaka, H. Morikawa, and R. Shimizu, J. Surf. Anal. **11**, 170 (2004).
[17] N. de Jonge and J. M. Bonard, Philos. Trans. R. Soc. London, Ser. A **362**, 2239 (2004).
[18] N. de Jonge, M. Allioux, M. Doytcheva, M. Kaiser, K. B. K. Teo, R. G. Lacerda, and W. I. Milne, Appl. Phys. Lett. **85**, 1607 (2004).
[19] H. B. Michaelson, J. Appl. Phys. **48**, 4729 (1977).
[20] P. J. Grundy and G. A. Jones, in *Electron Microscopy in the Study of Materials*, edited by B. R. Coles (Edward Arnold, London, 1976).
[21] S. Senda, M. Tanemura, Y. Sakai, Y. Ichikawa, S. Kita, T. Otsuka, A. Haga, and F. Okuyama, Rev. Sci. Instrum. **75**, 1366 (2004).
[22] G. H. N. Riddle, J. Vac. Sci. Technol. **15**, 857 (1978).
[23] A. Yamaguchi, M. Miyoshi, A. Haga, J. Kawashima, Y. Oga, and S. Kita (unpublished).
[24] Z. Liu, G. Yang, Y. Z. Lee, D. Bordelon, J. Lu, and O. Zhou, Appl. Phys. Lett. **89**, 103111 (2006).

J. Radiat. Res., 48, 153–161 (2007)

Regular Paper

Biological Effects of Field Emission-Type X-Rays Generated by Nanotechnology

Tomoharu NAKAZATO[1], Makoto NAKANISHI[2], Shigetomo KITA[3], Fumio OKUYAMA[3], Yuta SHIBAMOTO[4] and Takanobu OTSUKA[1]*

Field emission/X-ray/Nanotechnology/Carbon nanotube.

Thermionic emission (TE)-type X-ray generators have been exclusively used in medicine, but there are many difficulties in making these X-ray sources compact. A field emission (FE)-type X-ray generator using carbon nanotubes is a newly-developed compact system that can be as small as several cm in length. Considering the compactness of the equipment, the FE-type X-ray generator may become a useful tool for endoscopic, intracavitary or intraoperative radiotherapy in the future. The aim of this study was to investigate the biological effects of X-rays generated by the FE-type X-ray source in comparison with those of conventional TE-type X-rays. Mouse thymic lymphoma 3SB cells were irradiated by an FE-type X-ray generator developed by our group and a conventional TE-type X-ray source under identical conditions. DNA damage after radiation was detected by foci formation of phospho-H2AX (γ-H2AX). Effect on the cell cycle was analyzed by flow cytometry. Activation of the DNA damage checkpoint was analyzed by immunoblotting. Induction of apoptosis was studied using the TUNEL assay. In terms of induction of DNA damage (DNA double-strand breaks), activation of cell cycle checkpoints (p53 stabilization, p21 induction, Chk1 and Chk2 phosphorylations), and induction of apoptotic cell death, FE-type X-rays were as effective as TE-type X-rays, and FE-type X-rays appeared to be applicable to radiation therapy.

INTRODUCTION

For field emission (FE)-type X-ray sources, electrons striking a metal target are generated by a field emitting process, a quantum-mechanical process of electron tunneling (Fig. 1).

FE source has a protruding shape and is frequently (often, typically) made of "carbon nanotubes" (CNTs).[1)] Since electron tunneling critically depends on the chemical state of the electron-emitting surface,[2)] FE is unstable in non-ultrahigh vacuum (non-UHV) ambiences, especially for metallic cathodes that chemically react with gaseous molecules remaining in a non-UHV (Non-UHV ambience contains a large number of gaseous molecules, mostly H_2O molecules).

CNTs are helical microtubules of graphitic carbon, ranging from 4 to 30 nm in diameter and up to 1 mm in length.[3)] Chemically, carbon is far more stable than metals, and CNTs were therefore previously predicted to be promising FE sources.[4)] CNTs have recently been confirmed to field-emit electrons for a long period in X-ray tubes pumped down to a non- UHV.[5–8)]

Since FE requires no cathode heating, the entire tube structure of the FE-type X-ray generator could be miniaturized to be as small as several cm in length. Such a miniature X-ray tube,[9)] which is absolutely unattainable with conventional thermionic emission (TE)-type X-ray tubes,[10)] may play a role in clinical radiation therapy for the purpose of targeted X-ray irradiation to a superficial lesion. Since the FE-type X-ray source has been developed only recently by the group of Okuyama *et al.*,[1)] biological effects of the X-ray have not yet been investigated. Moreover, some differences have been proven to exist between FE- and TE-type X-rays with respect to energy spectra. Therefore, it is necessary to investigate whether biological effects of FE type X-rays are similar to those of TE type X-rays before consider-

*Corresponding author: Phone: +81-52-853-8236,
Fax: +81-52-842-0266,
E-mail: t.otsuka@med.nagoya-cu.ac.jp
[1]Department of Musculoskeletal Medicine; [2]Department of Biochemistry and Cell Biology and [4]Department of Radiology, Nagoya City University, Graduate School of Medical Sciences, 1 Kawasumi, Mizuho-cho, Mizuho-ku, Nagoya 467-8601, Japan; [3]Graduate School of Engineering, Nagoya Institute of Technology, Gokiso-cho, Showa-ku, Nagoya 466-8555, Japan.
Abbreviations. FE: Field emission. TE: Thermionic emission. CNT: Carbon nanotube
doi:10.1269/jrr.06071

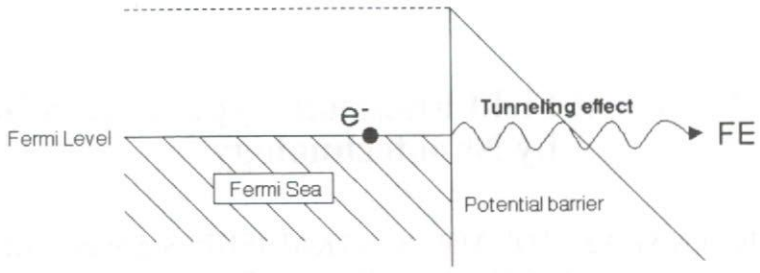

Fig. 1. Principle of FE (schematic). Electrons at the Fermi level penetrate the surface potential barrier that becomes thinner under a strong electric field.

ing their application in medicine.

X-ray is a representative agent causing DNA double-strand breaks (DSBs) of cells. Among the many types of damage, DSBs are the most deleterious to cell survival. To maintain genomic integrity, eukaryotic cells are equipped with coordinated systems to contend with DNA damage, including chromatin remodeling, cell cycle arrest, DNA repair and programmed cell death processes.[11–13] Numerous key players, including p53, p21, Chk1 and Chk2, have been identified, and their cooperation in damage control has only recently become evident. Therefore, it appeared meaningful to investigate the biological effects of FE-type X-rays using these endpoints.

In this paper, we present indisputable evidence that FE-type X-rays being emitted from a tungsten target damage DNA, activate cell cycle checkpoints and induce apoptosis in cancer cells cultivated *in vitro*.

MATERIALS AND METHODS

Cell culture

The mouse thymic lymphoma cell line 3SB was a gift from the National Institute of Radiological Sciences (Chiba, Japan).[14,15] The cells were maintained in RPMI 1640 medium (Sigma-Aldrich Inc., St. Louis, MO, USA) supplemented with 10% fetal bovine serum, penicillin (100 units/ml), streptomycin (100 mg/ml), and 10 mM HEPES Buffer Solution (Invitrogen Co., Grand Island, NY) at 37°C in a humidified 95% air-5% CO_2 atmosphere. The doubling time of 3SB cells was about 18 h *in vitro*. The cells were seeded at a density of $8\sim10 \times 10^5$ cells in 9.6 cm^2 plastic tissue culture dishes with 1.7 ml medium.

Treatment of the cells with nocodazole

The cells were synchronized at M phase with nocodazole at a concentration of 0.5 mg/ml for 8 h in an incubator and then incubated in a fresh medium for 3 h and irradiated (conditions determined by the results of a preliminary experiment). After these treatments, incubation was continued again.

Irradiation

The FE-type X-ray system was developed by the group of Okuyama *et al.* at Nagoya Institute of Technology (Nagoya, Japan). It is a slightly modified version of the X-ray system used in a previous study.[8,16] The conventional TE-type X-ray equipment was YXLON MG 226/2.25 (YXLON Int., Tokyo), and the X-ray tube was MCN 225 (Philips Industrial, Hamburg). It has been used for biological studies.[17,18] Characteristics of the two systems are summarized in Table 1.

Table 1. Characteristics of the field emission (FE)-type and thermionic emission (TE)-type X-ray sources.

Characteristic	FE-type	TE-type
Tube voltage (kV)	50	50
Current (mA)	1	1
Target	Tungsten	Tungsten
Window	Beryllium	Beryllium
Filter	None	None
X-ray spectra	Characteristic X-rays	Continuous
Source-to-object distance (cm)	12.5	18
Dose rate (Gy/min)	3.3 Gy/min	3 Gy/min
Dose inhomogeneity within samples	< 10%	< 3%

The X-ray spectra of the FE-type equipment obtained with Xfash Spectrometer (Röntec, Berlin, Germany) are shown in Fig. 2. As shown in the figure, the FE-type equipment generates characteristic X-rays almost exclusively, while conventional TE-type equipment with a tungsten target has been reported to generate continuous spectra with almost no peak of characteristic Xrays.[19]

Since the X-ray tube voltage of the FE-type system was 50 kV at maximum, both the FE-type and conventional TE-type sources were operated at 50 kV. Radiation doses were calibrated using a RAMTEC 1500B dosimeter (Toyo Medic, Tokyo, Japan) and a soft X-ray chamber (N 23344-0939, PTW-Freiburg, Germany). Fig. 3 shows the dose distribution

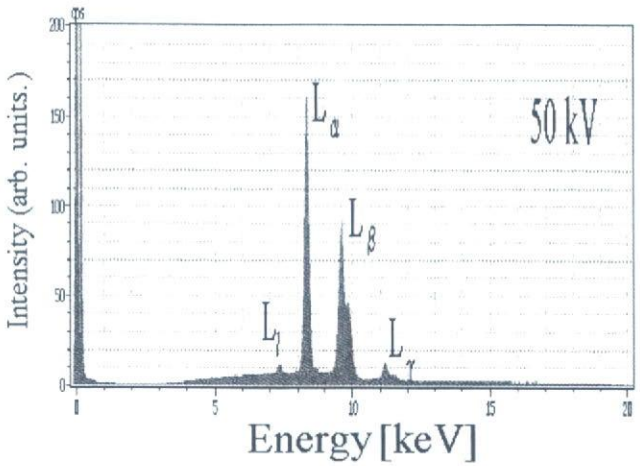

Fig. 2. Spectra of X-rays generated by the FE-type source.

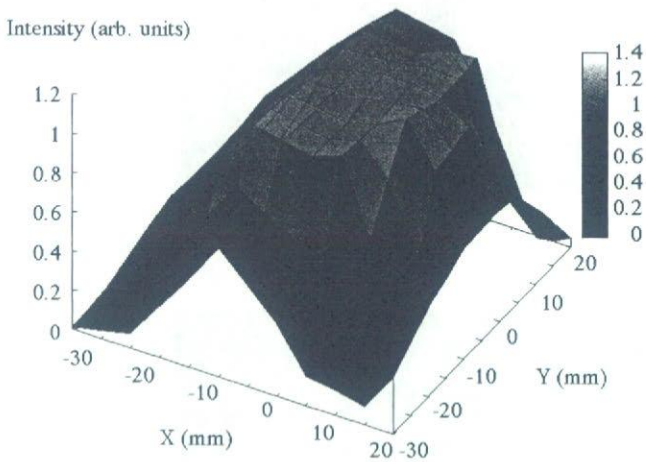

Fig. 3. Dose distribution of the FE-type X-ray (50 kV).

and homogeneity of the FE-type X-rays within the radiation field; in this experiment, culture dishes with an area of 9.6 cm^2 were used and dose inhomogeneity was therefore considered to be less than 10%. The lid of the culture dish was taken off during irradiation.

Immunofluorescence microscopy

After 1 h of 3 Gy irradiation, cells were harvested, washed twice in PBS, and fixed in 70% ethanol overnight at –20°C. After the cells had been washed and suspended in PBS at a concentration of 5×10^4/ml, cells in 500 µl PBS were attached to micro slide glasses using cytospin and the slide glasses were soaked in PBS. The soaked slides were permeabilized with PBS containing 0.2% Triton X-100 for 5 min and washed twice in PBS. Then they were blocked with 0.05% Tween 20 in 3% skim milk in PBS at room temperature for 1 h and rinsed in PBS. The slides were incubated at room temperature for 2 h with mouse monoclonal anti-γ-H2AX (Upstate Cell Signaling Solutions, Lake Placid, NY, 1:100) and for 1 h with Alexa Fluor® 488 goat anti-mouse IgG (H + L) (Molecular Probes Eugen, Oregon, USA, 1:1000). Finally, the cells were counterstained with 0.1 µg/ml 4'-6-Diamidino-2-phenylindole (DAPI) and analyzed using a fluorescence microscope, Nikon Eclipse E800 (Nikon Co., Kanagawa, Japan). Images were captured using a 100 × oil lens.

TUNEL assay

Nuclear DNA fragmentation of apoptotic cells was measured by the TUNEL assay (DeadEnd Fluorometric TUNEL System, Promega, Madison, WI). Briefly, irradiated cells were harvested, washed once in PBS, and resuspended in PBS at a concentration of approximately 5×10^4 /ml. Then cells in 500 µl PBS were attached to glass slides using cytospin, fixed in 4% formaldehyde, permeabilized in 0.2% Triton X-100, and incubated with TdT incubation buffer for 60 min in a 37°C humidified incubator for 3'-OH labeling. The cells were counterstained with 0.1 µg/ml DAPI and analyzed using a fluorescence microscope, Nikon Eclipse E800M at 40 ×. More than 200 cells per coded slide per time were scored for TUNEL labeling.

Flow cytometry

After radiation, cells were harvested, washed with PBS, and fixed in 70% ethanol over 4 h. They were counterstained with 50 µg/ml propidium iodide (PI) in PBS and analyzed using a flow cytometer and Cell Quest software (Beckton Dickinson Bioscience, San Jose, CA, USA).

Immunoblotting and antibodies

Irradiated cells were dissolved in solubilizing buffer (pH 8.0, 50 mM HEPES, 150 mM NaCl, 2.5 mM EGTA, 1 mM EDTA, 1 mM DTT, 0.1% Tween 20, 10% glycerol, and 5 mg/ml phosphatase substrate (Sigma 104®) with the addition of 1 mM sodium fluoride, 0.1 mM sodium orthovanadate and protease inhibitors such as 20 µg/ml soybean trypsin, 2 µg/ml aprotinin, 100 µg/ml PMSF, and 5 µg/ml leupeptin. Twenty µg of soluble proteins were separated by 10% sodium dodecyl sulfate-polyacrylamide gel electrophoresis. Separated polypeptides were then transblotted onto a PVDF membrane (Immobilin-P Transfer Membrane, Millipore Co., Billerica, Massachusetts) in transfer buffer (25 mM Tris base, 192 mM glycine, 25 mM sodium dodecyl sulfate, 10% methanol) at 100 V for 30 min at 4°C. Blots were then blocked with 5% skim milk in PBS/0.05% Tween 20 and incubated with the primary antibody at 1 µg/ml in 5% skim milk in PBS containing 0.05% Tween 20 for 1 h at room temperature. The secondary antibody was horseradish peroxidase-linked whole antibody, ECL™ anti-mouse immunoglobulin G or ECL™ anti-rabbit immunoglobulin G (Amersham Biosciences UK, Li., England) at 1:1000 in PBS/0.05% Tween 20. Signals were developed by ECL plus (Amersham Biosciences). Mouse monoclonal antibodies to p53 (Novocastra Laboratories Ltd., Newcastle

upon Tyne, UK) and to p21 (Santa Cruz Biotech, Inc., Santa Cruz, CA) and rabbit polyclonal antibodies to Chk2 (Santa Cruz Biotech.) and to Chk1 phosphorylated on Ser345 and on Ser317 (Cell Signaling Technology, Inc., Danvers, MA) were used. Equal sample loading was confirmed by reprobing the sample blots with mouse monoclonal antiserum against β-actin at 0.2 μg/ml (Abcam Inc., Cambridge, MA, USA), and the signal was developed by ECL™ (Amersham Biosciences).

RESULTS AND DISCUSSION

FE-type X-ray causes DNA damage as efficiently as TE-type X-ray does

H2AX is known to be a biological marker of DSBs caused by radiation and genotoxic reagents. To examine whether DSBs are actually induced by FE-type and TE-type Xrays, mouse thymic lymphoma 3SB cells were irradiated with FE-

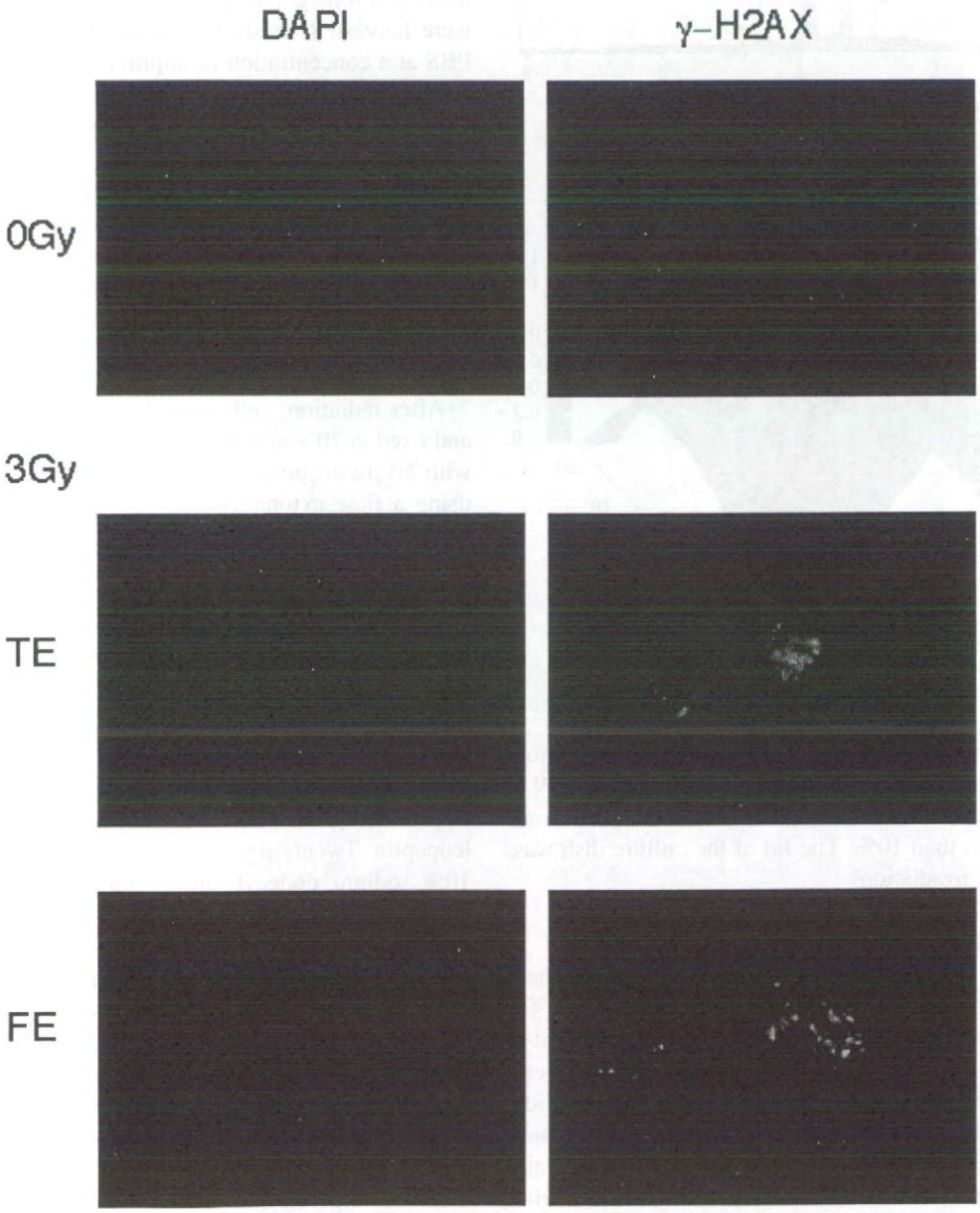

Fig. 4. DNA damage after radiation. One h prior to harvest, 3SB cells were treated with ionizing radiation. They were labeled with an anti-γ-H2AX antibody and then incubated with a secondary antibody and counterstained with DAPI. The labeled cells were imaged with a confocal microscope at 100 ×. X-ray type and dose are indicated on the left. DAPI staining and γ-H2AX staining are indicated at the top. Both TE and FE showed foci formation of γ-H2AX. Shown are representative micrographs of experiments carried out twice.

type or TE-type X-rays and the resultant DSBs were analyzed by foci formation of phospho-H2AX (γ-H2AX) using an antibody specific to γ-H2AX.[20,21] As shown in Fig. 4, foci formation of γ-H2AX was evident as early as 1 h after irradiation of FE-type X-rays (3 Gy), and the number of γ-H2AX foci in cells treated with FE-type X-rays was almost the same as that in cells treated with TE-type Xrays. Similar results were also obtained when cells were irradiated with 1 or 5 Gy (data not shown). Thus, these results indicated that FE-type X-rays are as effective as TE-type X-rays in terms of induction of DNA damage.

FE-type X-ray effectively activates the DNA damage checkpoint

We next determined the extent of DNA damage caused by FE-type or TE-type X-rays by examining cell cycle checkpoint activation because it is a highly sensitive assay for evaluation of the extent of DNA damage. The cell cycle of mouse lymphoma 3SB cells was arrested at G2/M phase but not at G1 phase when the cells were irradiated with either TE- or FE-type X-rays (data not shown). G2/M phase arrest by DNA damage is known to be regulated by checkpoint kinases, Chk1 and Chk2, in a PI3KK-dependent manner.[22–28] Therefore, we examined changes in the modification and the amount of proteins involved in G2/M arrest in response to DNA damage. Although cell cycle arrest at G1 phase was not evident upon DNA damage, the amount of p53 protein[29,30] was significantly increased and peaked at 3 h after irradiation of FE-type X-rays (Fig. 5a). The amount of p21 Cdk inihibitor protein, which is one of the p53 targets, was also increased, although it was a later event than p53 induction. The magnitudes of increase in amounts of p53

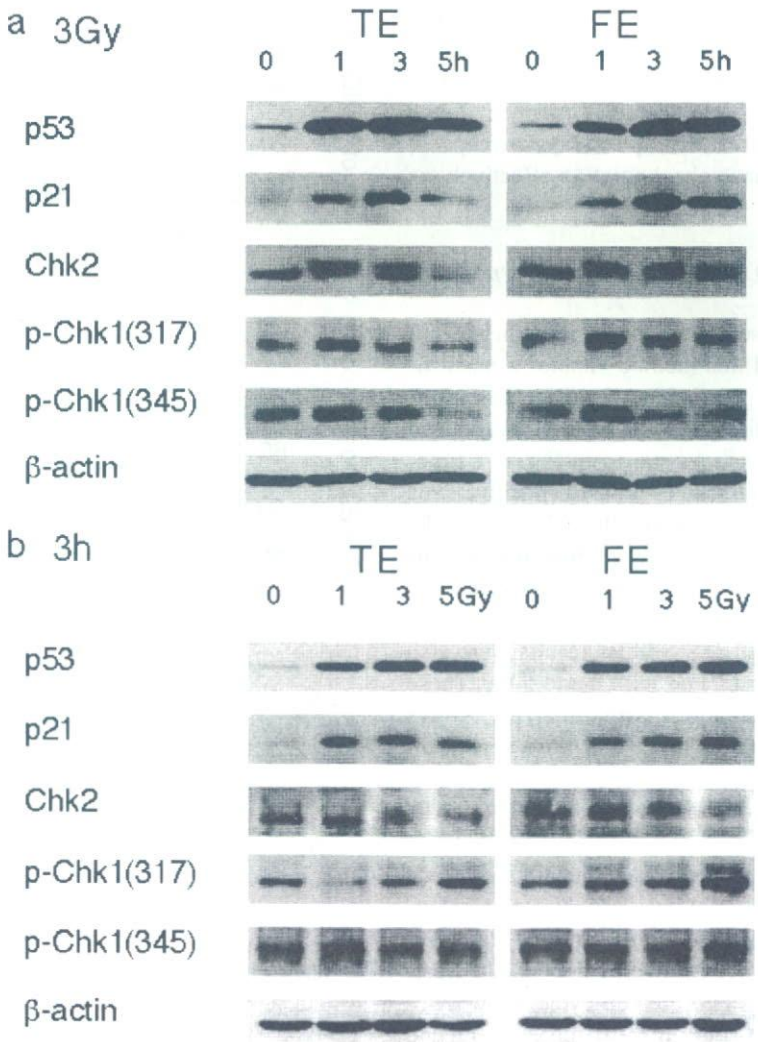

Fig. 5. Activation of DNA damage checkpoint after radiation. 3SB cells were exposed to TE- or FE-type X-rays at (a) 3 Gy or (b) indicated doses and harvested at (a) indicated times or (b) 3 h later. Cell lysates were subjected to immunoblot analysis with antibodies specific to p53, p21, Chk2, p-Chk1(317), p-Chk1(345) or, β-actin as indicated.

and p21 caused by FE-type X-rays were almost the same as those caused by TE-type X-rays.

Mobility shift of Chk2 bands[31] due to phosphorylation was also evident as early as 1 h and continued until 5 h after irradiation. Phosphorylaton of Chk1 was also examined using antibodies specific to phospho-Chk1 at Ser317 and phospho-Chk1 at Ser345. As shown in Fig. 5a, Chk1 was abruptly phosphorylated at both Ser317 and Ser345 at 1 h after irradiation and was then dephosphorylated. Importantly, the levels of phosphorylation of Chk2 and Chk1 in cells irradiated with FE-type X-rays were almost the same as those in cells irradiated with TEtype X-rays.

Furthermore, we examined the dose-dependency for modifications of checkpoint proteins by FE- and TE-type X-rays (Fig. 5b). Mouse 3SB cells were treated with the indicated dose of X-rays and then harvested at 3 h. Clear dose-dependent increases in the amounts of p53 and p21 proteins were observed in both cells irradiated with FE-type X-rays and cells irradiated with TE-type X-rays. Phosphorylations of Chk2 and Chk1 were also detected upon treatment with FE- and TE-type X-rays in a dose-dependent manner. Taken together, the results suggest that FE-type X-rays are capable of activating the DNA damage checkpoint as effectively as TE-type X-rays.

Induction of apoptosis by FE-type X ray is independent of cell cycle phase

The TUNEL assay is a useful tool for the identification of programmed cell death and this method enables a quantification of the process in cell populations. By using this assay, we examined whether irradiation of FE-type X rays indeed induced apoptotic cell death[32]. As shown in Fig. 6, a time-dependent increase in the number of TUNEL-positive cells was detected in 3SB cells treated with either FE-type or TE-type X-rays. TUNEL-positive cells were first detected as early as 1 h after 1 Gy irradiation (13.9 ± 0.6% with TE and 9.6 ± 0.6% with FE) and increased until 5 h (25.4 ± 2.7% with TE and 27.4 ± 2.2% in FE). Similar results were also obtained when cells were irradiated with 3 and 5 Gy. These results indicated that irradiation with FE-type X-rays induced apoptotic cell death in time- and dose-dependent manners and that the efficiency of FE-type X-rays for inducing apoptotic cell death was almost the same as that of TE-type X-rays.

Given that certain types of apoptotic cell death are known to be dependent on cell cycle progression,[33] we also examined whether this is also the case with FE-type X-rays. We synchronized the cell cycle at M phase by nocodazole treatment and then released cells into the cell cycle. Flow cytometric analysis revealed that cells entered S phase at 4 h and entered G2/M phase at 9 h after releasing.

As shown in Fig. 7, the population of subG1-phase cells significantly increased at 4 h and reached a maximum at 6 h after releasing. The increase in the population of subG1-phase cells upon treatment with FE-type X-rays was similar to that upon treatment with TE-type X-rays. Therefore, these results suggested that the induction of apoptosis by FE- and TE-type Xrays is at least in part dependent on S phase entry.

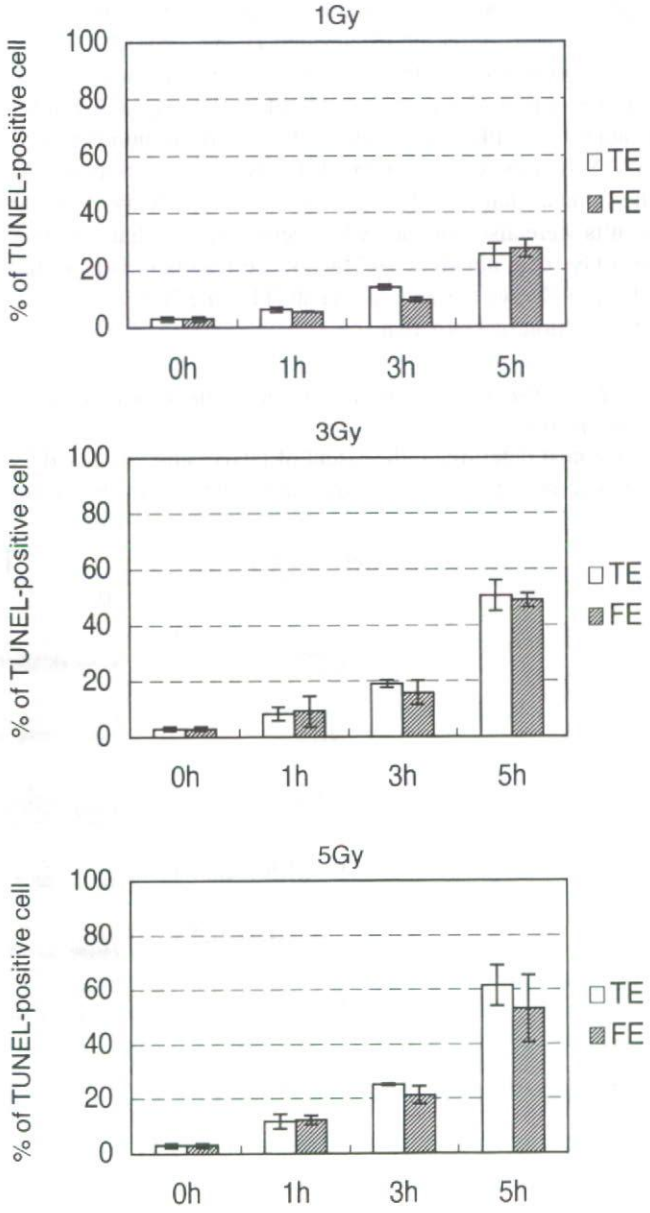

Fig. 6. Induction of apoptosis by radiation. (a) Cells were treated with TE-type (open bars) or FE-type (stippled bars) X-rays (indicated doses) and harvested at the indicated times thereafter. They were subjected to TUNEL analysis. The mean values of percentage of TUNEL-positive cells from two independent experiments are presented with error bars.

New type of radiation therapy may be developed in the future

This study has shown that FE-type X-rays from tungsten

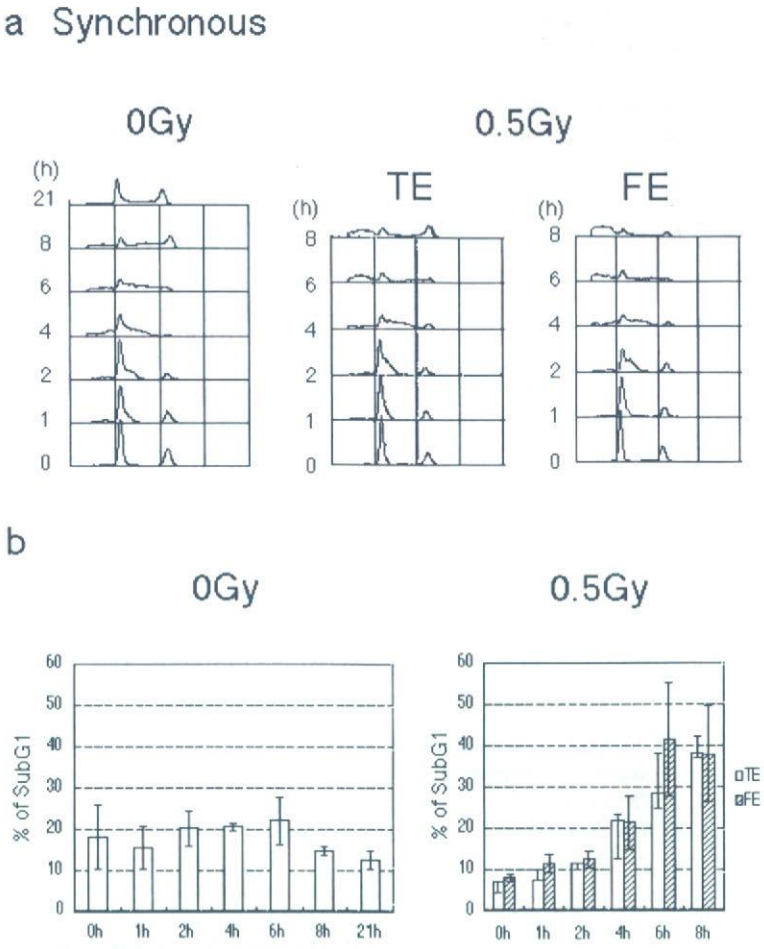

Fig. 7. Effect of X-rays on the cell cycle. (a) Representative histograms of synchronous 3SB cells exposed to TE- or FE-type X-rays (0, 0.5 Gy). Cells were treated with nocodazole. Cell cycle analysis was performed for cells harvested at the indicated times thereafter. (b) Cells were treated with nocodazole (upper panel) or in combination with exposure to TE-type (open bars) or FE-type (stippled bars) X-rays (0.5 Gy) (lower panel). The mean values of percentage of Sub G1 from two independent experiments are presented with error bars.

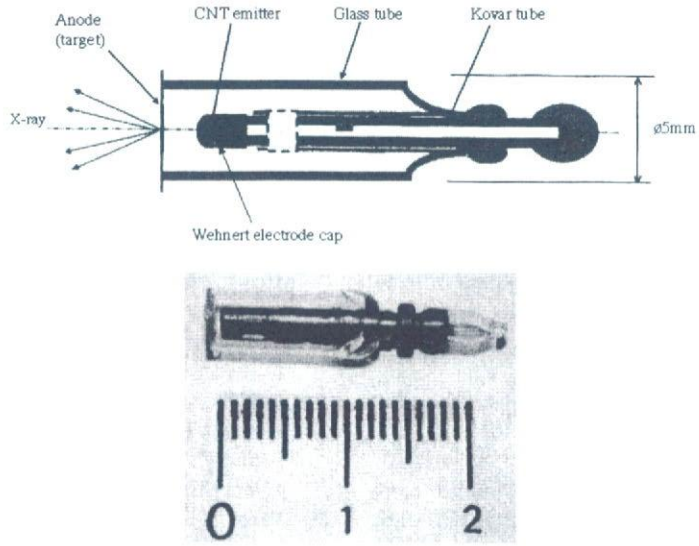

Fig. 8. A trial product of the miniature X-ray tube experimentally produced by Okuyama *et al.*[34] (reproduced with permission).

efficiently cause DNA damage and induce apoptosis in cancer cells.Hence, the FE-type X-ray generator may be applicable to cancer therapy. The entire tube structure of the FE-type X-ray source could be miniaturized as shown in Fig. 8. By coupling with an endoscope and narrowing the radiation field, such a miniature X-ray tube would pave the way to targeted X-ray irradiation of a tumor in the early stage or a superficial lesion and hence may lead to a new strategy for radiation therapy. Although the X-ray tube voltage (50 kV) is lower than conventionally used levels, the issue is practically insignificant and dose inhomogeneity (as shown in Fig. 3) may not be a problem in view of the smallness of lesions that are indicated for such treatment.

ACKNOWLEDGMENTS

We are grateful to Mr. Hiroyuki Niida and Mrs. Yuko Katsuno for technical assistance and to Mr. Masahiro Muto for preparing the 3SB cell line. This work was supported by 2004 Grants-in-Aid for Scientific Research awarded.

REFERENCES

1. Sugie, H., Tanemura, M., Filip, K., Iwata, K., Takahashi, K. and Okuyama, F. (2001) Carbon nanotubes as electron source in an X-ray tube. Appl. Phys. Lett. **78**: 2578–2580.
2. Fowler, R. H. and Nordheim, L. W. (1928) Electron emission in intense electric fields. Proc. Roy. Soc. London Ser. A **119**: 173–181.
3. Iijima, S. (1991) Helical microtubles of graphic carbon. Nature **354**: 56–58.
4. Collins, P. G. and Zettl, A. (1997) Unique characteristics of cold cathode carbon-nanotubematrix field emitters. Phys. Rev. **55**: 9391–9399.
5. Yue, G. Z., Qiu, Q., Gao, B., Cheng, Y., Zhang, Z., Shimada, H., Chang, S., Lu, J. P. and Zhou, O. (2002) Generation of continuous and pulsed diagnostic imaging of X-radiation using a carbon-nanotube-based field emission cathode. Appl. Phys. Lett. **81**: 355–357.
6. Matsumoto, T. and Mimura, H. (2003) Point X-ray source using graphite nanofibers and its application to X-ray radiography. Appl. Phys. Lett. **82**: 1637–1639.
7. Yamaguchi, A., Kobayashi, N., Aoki, N., Motoi, Y. and Mitsuoka, Y. (2004) Compact soft X-ray source for biological applications. Nucl. Sci. Symp. **N36**: 124–127.
8. Kita, S., Sakai, Y., Fukushima, T., Mizuta, Y., Ogawa, A., Senda, S. and Okuyama, F. (2004) Characterization of field-electron emission from carbon nanofibers grown on Pd wire. Appl. Phys. Lett. **85**: 4478–4480.
9. Haga, A., Senda, S., Sakai, Y., Mizuta, Y., Kita, S. and Okuyama, F. (2004) A miniature Xray tube. Appl. Phys. Lett. **84**: 5679–5681.
10. Endo, S., Hoshi, M., Takada, J., Takatsuji, T., Ejima, Y., Saigusa, S., Tachibana, A., Sasaki, M. S. (2006) Development, beam characterization and chromosomal effectiveness of X-rays of RTBC characteristic X-ray generator. J. Radiat. Res. **47**: 103–112.
11. Khanna, K. K. and Jackson, S. P. (2001) DNA double-strand breaks: signaling, repair and cancer connection. Nat. Genet. **27**: 247–254.
12. Geiman, T. M. and Robertson, K. D. (2002) Chromatin remodeling, histone modifications, and DNA methylation-how does it all fit together? J. Cell. Biochem. **87**: 117–125.
13. Vaziri, H., Squire, J. A., Pandita, T. K., Bradley, G., Kuba, R. M., Zhang, H., Gulyas, S., Hill, R. P., Nolan, G. P. and Benchimol, S. (1999) Analysis of genomic integrity and p53-dependent G1 checkpoint in telomerase-induced extended-life-span human fibroblasts. Mol. Cell. Biol. **19**: 2373–2379.
14. Ohyama, H., Muto, M. and Yamada, T. (1992) Apoptosis in newly established radiosensitive mouse lymphoma cell lines. Elsevier. Science. Publishers. 361–364.
15. Kawai, H., Yamada, Y., Tatsuka, M., Niwa, O., Yamamoto, K. I. and Suzuki, F. (1999) Down-regulation of nuclear factor κB is required for p53-dependent apoptosis in X-rayirradiated mouse lymphoma cells and thymocytes. Cancer Res. **59**: 6038–6041.
16. Senda, S., Tanemura, M., Sakai, Y., Ichikawa, Y., Kita, S., Otsuka, T., Haga, A. and Okuyama, F. (2004) New field-emission x-ray radiography system. Rev. Sci. Instrum. **75**: 1366–1368.
17. Ogino, H., Shibamoto, Y., Sugie, C and Ito, M. (2005) Biological effects of intermittent radiation in cultured tumor cells: influence of fraction number and dose per fraction. J. Radiat. Res. **46**: 401–406.
18. Sugie, C., Shibamoto, Y., Ito, M., Ogino, H., Suzuki, H., Uto, Y., Nagasawa, H and Hori, H. (2005) Reevaluation of the radiosensitizing effects of sanazole and nimorazole *in vitro* and *in vivo*. J. Radiat. Res. **46**: 453–459.
19. Purdy, J. A. (2004) Principles of radiologic physics, dosimetry, and treatment planning. In: Principles and Practice of Radiation Oncology 4th Edition, Eds. C. A. Perez, L. W. Brady, E. C. Halperin and R. K. Schmidt-Ullrich, pp. 180–218, Lippincott Williams & Wilkins, Philadelphia.
20. Rogakou, E. P., Pilch, D. R., Orr, A. H., Ivanova, V. S. and Bonner, W. M. (1998) DNA double-stranded breaks induce histone H2AX phosphorylation on serine 139. J. Biol. Chem. **273**: 5858–5868.
21. Yoshida, K., Yoshida, S. H., Shimoda, C. and Morita, T. (2003) Expression and radiationinduced phosphorylation of histone H2AX in mammalian cells. J. Radiat. Res. **44**: 47–51.
22. Rogakou, E. P., Boon, C., Redon, C. and Bonner, W. M. (1999) Megabase chromatin domains involved in DNA double strand breaks *in vivo*. Cell. Biol. **146**: 905–915.
23. Gatei, M., Sloper, K., Sörensen, C., Syljuäsen, R., Falck, J., Hobson, K., Savage, K., Lukas, J., Zhou, B. B., Bartek, J. and Khanna, K. K. (2003) Ataxia-telangiectasia-mutated (ATM) and NBS1-dependent phosphorylation of Chk1 on Ser-317 in response to ionizing radiation. J. Biol. Chem. **278**: 14806–14811.
24. Zhao, H. and Worms, H. P. (2001) ATR-mediated checkpoint pathways regulate phosphorylation and activation of human Chk1. Mol. Cell. Biol. **21**: 4129–4139.
25. Peng, C. Y., Graves, P. R., Thoma, R. S., Wu, Z., Shaw, A. S. and W. H. (1997) Piwnica, Mitotic and G2 checkpoint con-

trol: regulation of 14-3-3 protein binding by phosphorylation of Cdc25C on serine216. Science **277**: 1501–1505.
26. Matsuoka, S., Huang, M. and Elledge, S. J. (1998) Linkage of ATM to cell cycle regulation by the Chk2 protein kinase. Science **282**: 1893–1897.
27. Bartek, J., Falck, J. and Lukas, J. (2001) CHK2 kinase—a busy messenger. Nat. Rev. Mol. Cell. Biol. **2**: 877–886.
28. Abraham, R. T. (2001) Cell cycle checkpoint signaling through the ATM and ATR kinases. Genes. & Dev. **15**: 2177–2196.
29. Jack, M. T., Woo, R. A., Hirao, A., Cheung, A., Mak, T. W. and Lee, P. W. K. (2002) Chk2 is dispensable for p53-mediated G1 arrest but is required for a latent p53-mediated apoptotic response. PNAS. **99**: 9825–9829.
30. Levine, A. J. (1977) p53, the cellular gatekeeper for growth and division. Cell **88**: 323–331.
31. Gire, V., Roux, P., Thomas, D. W., Brondello, J. M. and Dulic, V. (2004) DNA damage checkpoint kinase Chk2 triggers replicative senescence. EMBO. J. **23**: 2554–2563.
32. Gavrieli, Y., Sherman, Y. and Sasson, S. A. B. (1992) Identification of programmed cell death in situ via specific labeling of nuclear DNA fragmentation. Cell. Biol. **119**: 493–501.
33. Bernhard, E. J., Maity, A., Muschel, R. J. and Mckenna, W. G. (1995) Effects of ionizing radiation on cell cycle progression. A review. Radiat. Environ. Biophys. **34**: 79–83.
34. Senda, S., Sakai, Y., Mizuta, Y., Kita, S. and Okuyama, F. (2004) Super-miniature X-ray tube. Appl. Phys. Lett. **85**: 5679–5681.

Received on August 27, 2006
1st Revision received on November 21, 2006
2nd Revision received on December 20, 2006
Accepted on January 11, 2007
J-STAGE Advance Publication Date: February 22, 2007

Journal of
Nanoscience and Nanotechnology
Vol. 8, 1–6, 2007

Tribological Properties of Single-Walled Carbon Nanotube Solids

Go Yamamoto[1,*], Toshiyuki Hashida[1], Koshi Adachi[2], and Toshiyuki Takagi[3]

[1] Fracture and Reliability Research Institute, Tohoku University, 6-6-11-707, Aza-Aoba, Aramaki, Aobaku, Sendai 980-8579, Japan
[2] Graduate School of Engineering, Tohoku University, 6-6-01, Aza-Aoba, Aramaki, Aobaku, Sendai 980-8579, Japan
[3] Institute of Fluid Science, Tohoku University, 2-1-1, Katahira Aoba-ku Sendai, 980-8577, Japan

Binder-free single-walled carbon nanotube (SWCNT) solids were evaluated for solid lubrication applications. The steady-state friction coefficients (μ) for the SWCNT solids were found to reach values as low as 0.22–0.24, according to unidirectional sliding friction tests using Si_3N_4 counterparts in air. The values were slightly higher than that of bulk graphite material ($\mu = 0.20$). SEM and Raman analyses showed that most SWCNTs that existed in the friction surface transformed into SWCNT-derived transferred film made up of amorphous carbon during sliding. The resultant friction behavior may be related to the smearing of transferred film over the contact area, which was expected to permit easy shear and then help to achieve a lubricating effect during sliding.

Keywords: Single-Walled Carbon Nanotube, Solid Lubrication, Tribological Properties, Transferred Film.

1. INTRODUCTION

Due to the great changes in technology that have occurred in the last century, a larger number of components fabricated in engineering materials have been used, attaining in many cases better advantages such as reduction of maintenance costs, improvements in durability and reliability.[1] A high friction coefficient can greatly deteriorate the durability and reliability of a tribosystem, therefore, means of reducing the friction coefficient must be taken during most practical applications. A low friction coefficient can usually be achieved by liquid and gas lubrication,[2,3] although these lubricants cannot be used at elevated temperatures or in vacuum environments. In such cases, solid lubricants may be useful to lower the friction coefficient so as to meet the operational needs.

It is known that carbon-derived materials such as graphite and diamond-like carbon (DLC) have outstanding lubrication properties, which have been widely used as solid lubricants for many years. Graphite is one of these common solid lubricants, for it has a layer lattice structure with weak van der Waals bonding between the layers that can permit easy shear and then result in a low friction coefficient. For this reason, solid lubricants containing graphite have proved to be efficient under conditions where conventional lubricants are unstable or ineffective. Other similar carbon-derived materials such as fullerenes, carbon nanohorns (CNHs) and carbon nanotubes (CNTs) may be strong candidates for possible application to solid lubricants. A significant amount of research has been done on the tribological properties of C_{60} fullerene. Due to its unique spherical and highly symmetric structure, C_{60} was anticipated as nanoscale ball bearing to act as a good solid lubricant.[4] Nevertheless, according to previous reports,[5,6] C_{60} film seem to give higher friction coefficients than graphite and DLC. Tanaka et al.[7] reported that the friction coefficient of the CNH-containing polyimide composites, having 10 mass% of CNH, decreased by nearly half compared to CNH-free monolithic polyimide synthesized under similar processing conditions, but which value was somewhat higher than that of the composite with 10 mass% graphite.

CNTs are also presently being investigated for solid lubrication applications. Previous studies on the tribological properties of CNTs were mostly done with CNT-containing composites.[8–12] Improvements in friction and wear properties were frequently observed due to the reinforcement supplied by high-aspect-ratio CNTs. However, CNTs are also still in the early stages of development in the field of tribology, and it will be some time before practical tribological usage is realized. A fundamental understanding of the tribological properties of CNTs is the first step to understanding how the CNTs might react to the friction surface.

In our previous report,[13,14] we succeeded in preparing binder-free macroscopic single-walled carbon nanotube

*Author to whom correspondence should be addressed.

RESEARCH ARTICLE

1533-4880/2007/8/001/006 doi:10.1166/jnn.2007.295